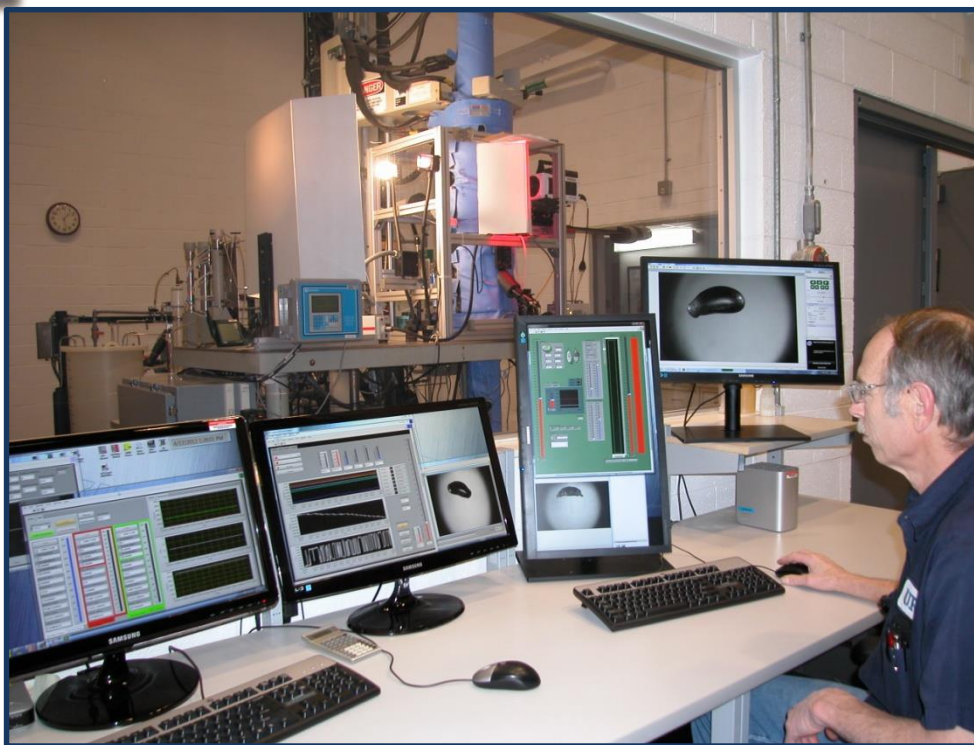


NATIONAL ENERGY TECHNOLOGY LABORATORY



The Role of Gas Hydrates during the Release and Transport of Well Fluids in the Deep Ocean

DOI/BSEE Contract E12PG00051/M11PPG00053

Final Report

December 31, 2014

Robert P. Warzinski, PI

Current Participating Organizations

URS
West Virginia University

Past Participating Organizations

Colorado School of Mines Center for Hydrate Research
(Amadeu Sum, PI)

This study was funded in part by the U.S. Department of Interior, Bureau of Safety and Environmental Enforcement through Interagency Agreement E12PG00051/M11PPG00053 with the Department of Energy, National Energy Technology Laboratory.



Table of Contents

Team Members	3
Introduction.....	3
Summary of Accomplishments.....	4
Research Plan Execution Summary	4
Experimental Method.....	5
Equipment and gases.....	5
Method	8
Experimental Results with CH ₄ and the C1C2C3 Gas Mixture.....	10
Overview of CH ₄ data	10
Overview of C1C2C3 data.....	13
Effect of gas saturation on initial hydrate formation	17
Effect of gas saturation on bubble dissolution.....	17
Effect of temperature on bubble dissolution.....	20
Effect of pressure on bubble dissolution.....	21
Effect of salinity on bubble dissolution	22
Effect of hydrate on bubble dissolution	24
Effect of COREXIT EC9500 on bubble dissolution and hydrate formation.....	27
Effect of hydrate morphology on bubble dissolution	29
Effect of hydrate on rise velocity.....	31
Bubble swarms and hydrate formation.	33
Thermodynamic and Bubble Plume Modeling.....	35
Development of a thermodynamic model for sII hydrates	35
Hydrocarbon bubble transport and fate modeling	36
Research Needs.....	48
Publications and Presentations.....	50
References	51
Abbreviations and Symbols	53

(Cover Photo: M. Schellhaas at the NETL High-pressure Water Tunnel Facility)

Team Members

Robert P. Warzinski, PI, NETL-ORD, Research Chemist
 Franklin Shaffer, NETL-ORD, Mechanical Engineer
 Ronald Lynn, NETL/URS, Engineer
 Dr. Igor Haljasmaa, NETL/URS, Mechanical Engineer
 Michael Schellhaas, NETL/URS, Engineering Technician
 Dr. Brian Anderson, NETL/RUA (WVU), Chemical Engineer
 Srinath Velaga, NETL/RUA (WVU), Chemical Engineering Graduate Student
 Dr. Ira Leifer, UCSB, MSI, ORISE, Atmospheric Scientist
 Dr. Jonathan Levine, NETL, ORISE, Earth and Environmental Engineering

Introduction

Attempts to mitigate the unprecedented massive release of fluids from the damaged BP Deepwater Horizon Macondo well in the Gulf of Mexico highlighted the need to accelerate research in multiple areas associated with improving safety in exploration and production in such demanding environments. One critical area is a lack of fundamental information on the role of natural gas hydrates during the release and transport of well fluids in the deep ocean.

This project involved the use of existing, novel equipment to obtain fundamental, crosscutting chemical, physical, and hydrodynamic information on gases that could be released and transported from subsea hydrocarbon reservoirs and inadvertently released into a deepwater environment. The specific objective of the research is to provide this fundamental information for use in numerical, thermodynamic, and plume models to comprehensively describe potential roles and impacts of gas hydrates in such a scenario. The goal is to facilitate a more comprehensive understanding of: (1) The formation and stability of simple and complex hydrates under deepwater conditions; (2) The stability of hydrates and their interaction with hydrocarbon fluids at or near the point of release into deep water and at longer times as they are transported away from the point of release into the seawater column; and (3) The impact of dispersants on the fate and interaction of hydrates near the point of release and during transport in the seawater column.

In the first year of performance, this project leveraged the strengths of two organizations, the Department of Energy's (DOE) National Energy Technology Laboratory (NETL) and the Colorado School of Mines (CSM) Center for Hydrate Research (CHR), both known for their long-term commitment to the development of safe energy exploration, development, and delivery technologies. Both organizations also have a long track record of research on relevant gas hydrate phenomena and application of fundamental and applied concepts to industrial practice and safety in such environments. Financial support from the CSM-CHR unfortunately had to end during the first year due to funding constraints and personnel factors beyond their control. During this interval, Dr. Jonathan Levine was supported by CSM-CHR. After this, Dr. Levine was funded at NETL through the Oak Ridge Institute of Science and Engineering (ORISE) using funding from the DOE Complementary Research Program under Section 999 of the Energy Policy Act (EPA) of 2005.

This final report is structured to contain summaries of the experiments performed, the thermodynamic modeling, and the development of an improved bubble plume model. Several appendices are included that contain the actual experimental data and detailed bubble dissolution analysis results.

Summary of Accomplishments

The following highlights accomplishments of this research, which are further described in the rest of the report and appendices.

- An extensive set of bubble observations were performed in NETL's High-Pressure Water Tunnel Facility (HWTF) using methane (CH₄), a structure I (sI) hydrate former, and a methane/ethane/propane mixture (C1C2C3), a structure II (sII) hydrate former, in both water prepared by reverse osmosis (RO) and 35 salinity artificial seawater at conditions ranging from 1 to 13°C, 500 to 3000 m simulated depth, and elevated levels of dissolved gas. A subset of experiments were performed with C1C2C3 in seawater containing 200 ppm of the COREXIT EC9500 dispersant. These experiments revealed the following:
 - Initial hydrate formation (no memory effect) on a bubble required the system to be supersaturated with respect to predicted levels of dissolved gas required for liquid/hydrate (LH) equilibrium. The degree of super-saturation increased with temperature. The increase was less for C1C2C3 than for CH₄.
 - Once hydrate forms on a bubble it is stable at lower pressures. Complete decomposition of the hydrate occurs as the vapor/liquid/hydrate (VLH) equilibrium pressure for the gas at the temperature of the system is approached.
 - New insights were gained into hydrate morphology on the surface of a gas bubble and the interaction of bubble hydrodynamics on the surface morphology.
 - The interaction between surficial bubble hydrates and bubble hydrodynamics is analogous to similar interactions between sea ice and wave dynamics.
 - Surficial bubble hydrates reduce bubble dissolution, with an inverse linear relation indicated between the extent of hydrate coverage and bubble shrinkage rate due to gas dissolution.
 - Bubble rise velocity can be decreased by hydrate formation on its surface.
- A thermodynamic model with no adjustable parameters was developed to predict both VLH and LH equilibrium conditions for gases of interest in both water and seawater.
- Results from the thermodynamic model were utilized in a bubble plume model to illustrate the fate of deep-sea gas releases as they are transported through the water column and even into the atmosphere. The role of hydrate formation in facilitating transport of gases to shallower depths and even into the atmosphere was clearly demonstrated in this work.

Research Plan Execution Summary

The research was guided by the tasks in the original Gantt chart shown in Figure 1. Experimental results obtained during the first year of research on Task 2 led to a decision by the Team and the Bureau of Safety and Environmental Engineering (BSEE) to extend work on Task 2 at the expense of time devoted to experiments on Task 3. Research was therefore not performed with oil and anti-agglomerants. However, research was performed with C1C2C3 and the COREXIT EC9500 dispersant.

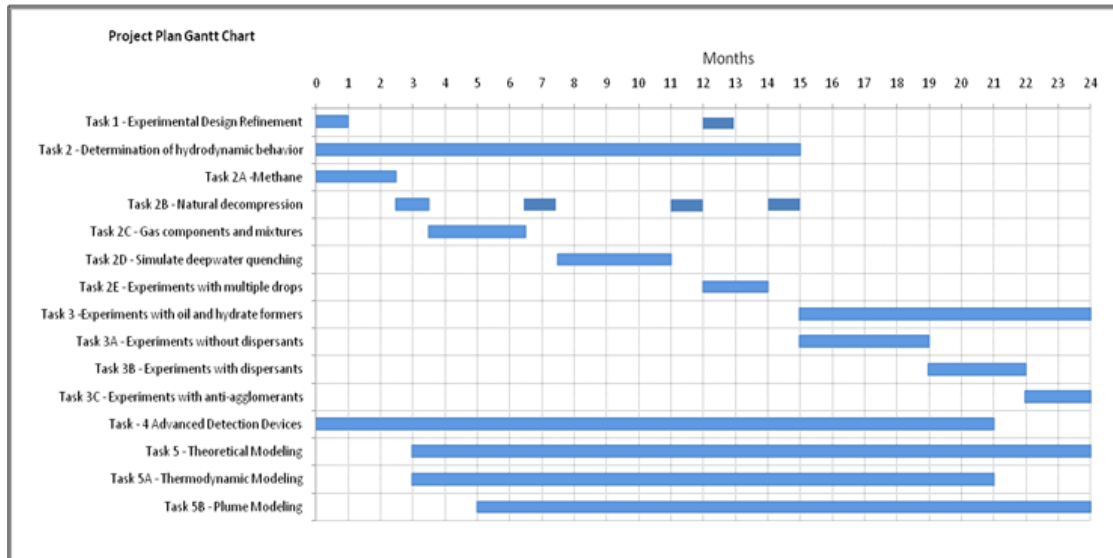


Figure 1. Original Gantt chart taken from the project proposal submitted to BSEE in April, 2011.

Task 4 was originally the responsibility of CSM-CHR and initial work was performed while they were able to participate in the project. Additional research was performed on a separate but complimentary project with the support from the DOE EAct Section 999 Complimentary Research Program utilizing data obtained from the HWTF. Part of this research resulted in a NETL Technical Report entitled “Detection of Hydrates on Gas Bubbles during a Subsea Oil/Gas Leak,” which focused on information useful for the development of a video-based, ROV-deployable system for qualitative and perhaps quantitative determination of the presence of hydrate on rising gas bubbles from a subsea hydrocarbon leak. This report has been submitted to NETL management in draft form. Thermodynamic modeling and bubble plume modeling aspects of Task 5 were both completed successfully.

Experimental Method

Equipment and gases

The experimental work reported here was performed in the NETL high-pressure water tunnel facility (HWTF). A picture of the HWTF is shown in Figure 2 and a flow schematic in Figure 3. Figure 3 shows the main components of the HWTF as indicated in the legend. Additional operation details have been published (*Haljasmaa*, 2005, 2006; *Warzinski et al.*, 2008).

The HWTF was designed to study rising or sinking fluid or solid particles at deep ocean conditions, simulating water depths to 3400 m and temperatures down to freezing. A vertical, countercurrent water flow is used to stabilize the fluid or solid particle(s) in a windowed viewing region for minutes to hours while video-based measurements are made. Vertical positioning of a particle in a window of a viewing section (VS in Figure 3) is achieved by countering its natural buoyancy with a controlled water flow through a tapered, conical, plastic insert in the VS that causes the water velocity to decrease with increasing diameter of this insert.

The inside dimensions of the tapered conical insert are represented in Figure 3. Straight plastic inserts are used in the distributor plates (DP) and stilling sections (SS) of the water tunnel. A

custom cylindrical flow conditioner (Figure 3 inset), made from a plastic honeycomb block, located upstream of the VS creates a velocity minimum near the vertical axis of the VS that provides radial stabilization of a particle in the VS. Particles up to about 20 mm diameter have sufficient freedom to permit a measure of natural hydrodynamics to be observed, in particular, wake-induced lateral path and shape oscillations.

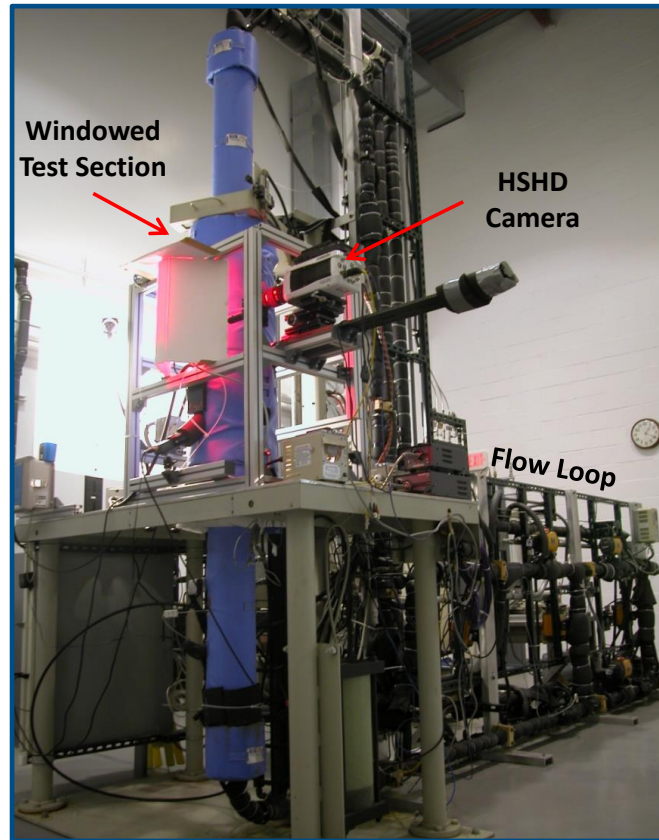


Figure 2. The NETL High-Pressure Water Tunnel Facility showing the water tunnel in blue insulation, the central windowed viewing section (larger diameter), the high-speed, high-definition (HSHD) camera, and the liquid flow loop.

A promotional video of the HWTF made by NETL can also be viewed at:

<https://www.youtube.com/watch?v=hCSPkevMB1w>

This video shows the HWTF facility in simulated operation, i.e., prerecorded bubble images on screens and with the system at ambient conditions owing to safety factors prohibiting unauthorized personnel in the facility while in pressurized operation.

The bright red LED lighting shown on the HWTF windowed test section in Figure 2 was employed to prevent the bright white lights used for the HSHD camera (opposite this camera and reflecting off the whiteboard to the left of the windowed test section) from interfering with a separate bubble tracking camera (opposite the red LED and 90° counterclockwise from the HSHD camera in the horizontal plane) that was equipped with a red filter. The HSHD camera, a Phantom v341 from Vision Research, operates mainly in the blue part of the visible light spectrum and is not affected by the red lighting.

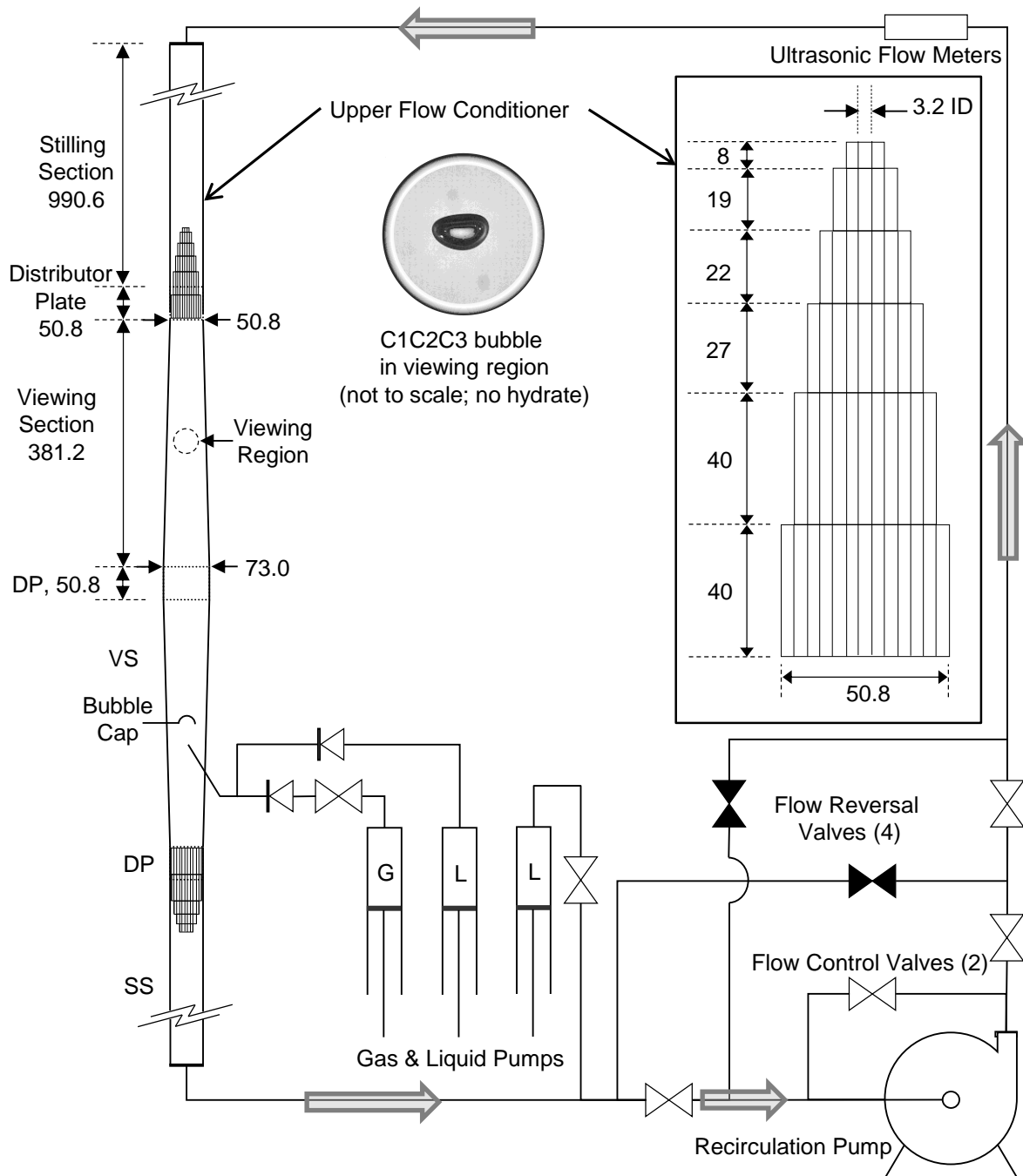


Figure 3. Schematic of the high-pressure water tunnel facility showing the water tunnel on the left and the typical flow used to stabilize a rising gas bubble in a viewing region. Dimensions in mm. The water tunnel (WT) consists of two windowed viewing sections (VS) that each contain in the viewing region two opposed 38.1 mm diameter circular windows and two opposed 12.7 mm by 152.4 mm oblong windows that are orthogonal to the circular windows, two stilling sections (SS), and three distributor plates (DP) that join these sections and provide various access ports. The diagram only shows the interior geometry of the WT, the stainless steel pressure shell is omitted. The top center inset shows a C1C2C3 bubble stabilized in the HWTF by a downward flow of water. The upper left insert shows the detail of the upper flow conditioning element used to provide radial stabilization of a bubble in the VS.

Bubbles of gas of about 10 to 15 mm diameter were formed in the experiments reported here by introducing a slow stream of smaller bubbles (~3 mm) from a syringe pump (lower left of Figure 3) into an inverted bubble cup in the lower VS of the HWTF. Another liquid syringe pump was used to flush any remaining bubbles in the injection line into the bubble cup. After the bubbles rapidly coalesced they were released and rose into the upper VS where a downward flow of water was adjusted to maintain the bubble in the viewing region. Pressure was simultaneously increased to the desired experimental pressure through the use of another liquid syringe pump that monitored the pressure in the HWTF and adjusted the water volume to maintain a set pressure. Teledyne Isco 260D syringe pumps were used for liquids and a model 100DM was used for gas bubble injection.

Temperature and pressure were measured with an Omega platinum RTD and a Heise ATS2000 digital pressure transducer, respectively. The RTD was located in the middle DP (Figure 3) and penetrates the plastic insert. The pressure transducer was connected to a port in the lower DP. The accuracy and a discussion of relevant measurement errors for these devices have been reported [Warzinski et al., 2014, supporting information].

The experimental work was performed primarily with either 99.996% methane (CH₄) or a mixture of ethane (8.121%) and propane (4.448%) with the balance methane (C₁C₂C₃) in either water treated by reverse osmosis (RO water) or artificial seawater made from Instant Ocean® with a salinity of 35 as determined by a PINPOINT® salinity monitor calibrated against a 53 mS calibration fluid, both from American Marine, Inc.

Method

A typical experiment involved observing bubbles as a function of temperature (T), pressure (P), dissolved gas concentration (X), and salinity (either RO water or 35 salinity artificial seawater). Pressure can typically be changed and stabilized in less than three minutes by adding or withdrawing water from the syringe pump that is connected to the HWTF flow loop (Figure 3). A recirculating chiller provides coolant to the entire facility that is used to both cool and heat the HWTF. Temperature change is possible over minutes to hours depending on the magnitude of the change. Cooling from ambient temperature to experimental set points can take up to 4 hours and is done overnight whenever possible. The HWTF viewing sections have connected machined channels for coolant flow while the rest of the HWTF is traced with copper cooling lines. Dissolved gas concentration is increased by the addition of gas from a syringe pump and, depending on the magnitude of the increase can be done in about an hour or more. Dissolved gas concentration cannot be reduced other than by complete degassing of the fluid in the HWTF. Salinity was only varied with a complete change of the aqueous phase in the HWTF.

A typical experimental series is started with either RO water or seawater in the HWTF and the temperature equilibrated to the first desired value, usually the lowest in the series. No dissolved gas is present in the system unless the experimental series started at an elevated level. Individual bubble observations are performed at different pressures, typically at 10, 20 and 30 MPa; which simulate depths of 1000, 2000, and 3000 m, respectively. The objective of the experiments is to determine the behavior of the bubble, which includes hydrodynamic behavior, dissolution rate, and the thermodynamics and kinetics of hydrate formation and dissociation.

Figure 4 depicts a plot of the vapor/liquid/hydrate (VLH) equilibrium and liquid/hydrate (LH) equilibrium for CH₄. Hydrate cannot form and melts below VLH equilibrium. Hydrate also would dissociate into the liquid phase at conditions of dissolved gas saturation that are to the left of the LH equilibrium lines.

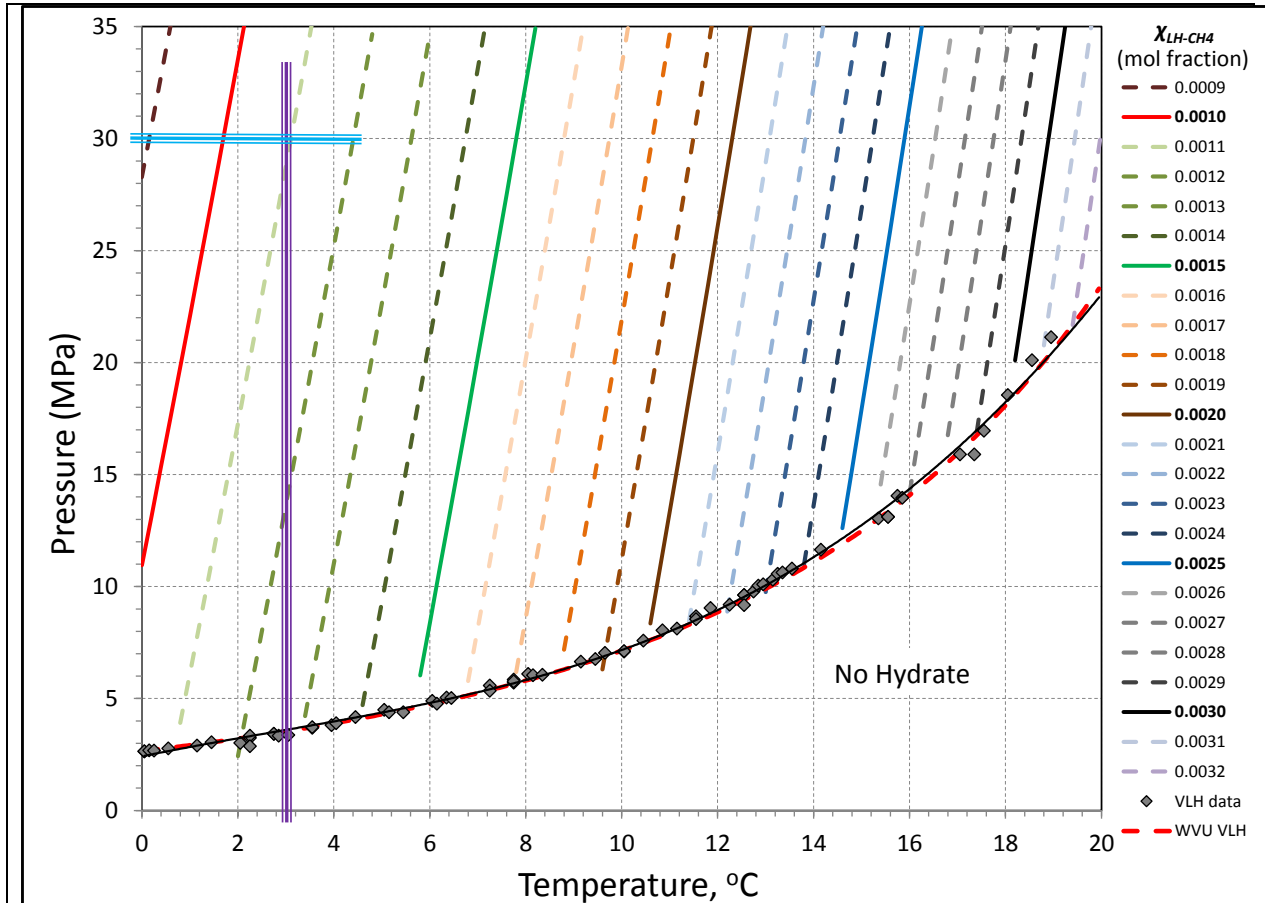


Figure 4. The vapor/liquid/hydrate (VLH) and liquid/hydrate (LH) equilibria for CH₄ in RO water using the experimental VLH data reported in *Sloan and Koh* (2008), represented by the black diamond data points and polynomial fit, and a correlation based on the experimental LH data of *Lu et al.* (2008), represented by the diagonal dashed and solid lines, which are color keyed to the legend at the right. Pressure is absolute. The dashed red line (WVU VLH) represents data calculated using a model developed on this project by team members from West Virginia University and show excellent agreement with the experimental data.

As shown in Figure 4, a typical bubble observation is conducted at a set temperature, 3°C in this example. Step increases in X_{CH_4} are made between bubble observations to approach the equilibrium concentration related to LH equilibrium at the temperature of the experiment. In Figure 4, the vertical purple and horizontal blue lines show that at 3°C and 30 MPa, respectively, hydrate can form from dissolved CH₄ gas if $X_{LH} \geq 0.0011$ mol fraction.

In Figure 4 the level of dissolved gas required for hydrate stability is observed to increase with increasing temperature and decrease with increasing pressure. Experiments that typically started

at lower temperatures could continue with observations of bubble hydrate processes by going to a higher temperature. Referring to Figure 4, if the temperature was increased to 8°C, at 30 MPa the required dissolved gas concentration for hydrate stability would then be slightly over 0.0015 mol fraction.

Experimental Results with CH₄ and the C1C2C3 Gas Mixture

Overview of CH₄ data

Experiments with CH₄ were performed during this project during three different time periods. The initial and largest set of experiments was performed from 5/8/12 through 7/6/12, the next from 10/15/12 through 11/2/12, and the last from 6/24/14 through 7/3/2014. Most of these experiments were performed in RO water. The rationale for this decision was based on the fact that high-quality data were available in the peer-reviewed literature for this system, in particular, the data of *Lu et al.* (2008), on the effect of dissolved gas on hydrate stability. Moreover, the *LU et al.* (2008) data set was validated in a review by *Thibodeaux et al.* (2011).

Table 1 summarizes the individual methane bubble observations in RO water.

Table 1. Summary of individual CH₄ bubble observations in fresh water in the HWTF.

T, °C	1 to 3		4 to 6		7 to 9		10 to 13	
X _{CH₄}	0 to 0.00122		0 to 0.00151		0 to 0.00216		0.00212 to 0.00213	
Depth, m (psia) ↓	NH	H	NH	H	NH	H	NH	H
500-650 (740-957)	2	-	-	-	-	1	-	-
650-750 (957-1102)	1	-	-	-	6	-	-	-
750-1000 (1102-1465)	-	-	4	2	3	-	-	-
1000 (1465)	11	3	7	1	7	2	1	-
1500 (2190)	2	-	-	-	-	-	-	-
2000 (2915)	8	-	7	1	6	1	1	-
2500 (3641)	2	-	-	-	-	-	-	-
3000 (4366)	16	3	6	3	17	3	2	-
Total bubbles	42	6	24	7	39	7	4	-

Table Notes

- X_{CH₄}: Mole fraction of methane dissolved in the water in the HWTF.
- NH and H: No Hydrate formed and Hydrate formed, respectively. The numbers below these headings represent the number of individual bubbles injected and observed.
- The conditions in the table represent initial conditions.
- 129 individual bubbles were injected and released into the HWTF.
- 109 individual bubbles were hydrate free during observation.
- 20 bubbles formed hydrate during or after injection.
- 16 cycles were performed to melt hydrate by stepwise depressurization.
- 12 cycles were performed to form hydrate by stepwise pressurization.

Table 2 summarizes experiments conducted with individual methane bubbles in artificial seawater. These experiments were performed from 7/9/2014 through 7/31/2014.

Table 2. Summary of individual CH₄ bubble observations in 35 salinity artificial seawater in the HWTF.

T, °C	1 to 3		4 to 6		7 to 9		10 to 13	
X_{CH4}	0 to 0.00115		0.00115 to 0.00152		0.00152 to 0.00154		0.00155	
Depth, m (psia) ↓	NH	H	NH	H	NH	H	NH	H
1000 (1465)	2	1	3	-	1	-	-	-
2000 (2915)	2	-	2	-	-	1	-	-
3000 (4366)	2	1	8	3	-	1	-	1
Total bubbles	6	2	13	3	1	2	-	1

Table Notes

- X_{CH4} : Mole fraction of methane dissolved in the water in the HWTF.
- NH and H: No Hydrate formed and Hydrate formed, respectively. The numbers below these headings represent the number of individual bubbles injected and observed.
- The conditions in the table represent initial conditions.
- 28 individual bubbles were injected and released into the HWTF.
- 20 individual bubbles were hydrate free during observation.
- 8 bubbles formed hydrate during or after injection.
- 6 cycles were performed to melt hydrate by stepwise depressurization.
- 3 cycles were performed to form hydrate by stepwise pressurization.

The experimental conditions and dissolution rate results for all of the work with CH₄ are contained in 7 chronologically ordered data sets in Appendix A. These data sets also are accompanied by a figure or figures that illustrate the strategy of most of the experimental series, which was to incrementally increase the dissolved gas concentration (X_{exp}) until hydrate formation occurred on a bubble. At each X_{exp} , especially early ones when X_{exp} was below the predicted LH equilibrium concentration for hydrate to form, individual bubbles were released at different pressures, typically those corresponding to ocean depths of 1000, 2000, and 3000 m. Temperature was typically held constant during each set; however, it was increased in the latter part of three of the seven sets to move the system to a state with a higher X_{exp} at LH equilibrium, i.e., less favorable for hydrate formation. A new experimental series (data set) was initiated when the HWTF was depressurized and the water either exchanged or degassed, effectively starting the next series with no dissolved gas.

An example experimental series is shown in Figure 5 below. An explanation of the various symbols and axes are in the figure caption.

In Figure 5, the experimental sequence involved individual bubble observations at different pressures with little variation in temperature. The dissolved gas concentration was progressively increased in steps to promote hydrate formation. Gas was added after Observations #3, #5, #7, #9, and #11

Changes in P_{exp}/P_{LH} in Figure 5 are mostly due to the changes in pressure, with the highest pressure ratios being near 30 MPa (a $P_{exp}/P_{VLH} \approx 10$). At these highest pressures, the effect of small variations in T on P_{exp}/P_{VLH} is evident in Observations #4 through #11. The observations represented in this figure were all conducted in the 1 to 3°C temperature range.

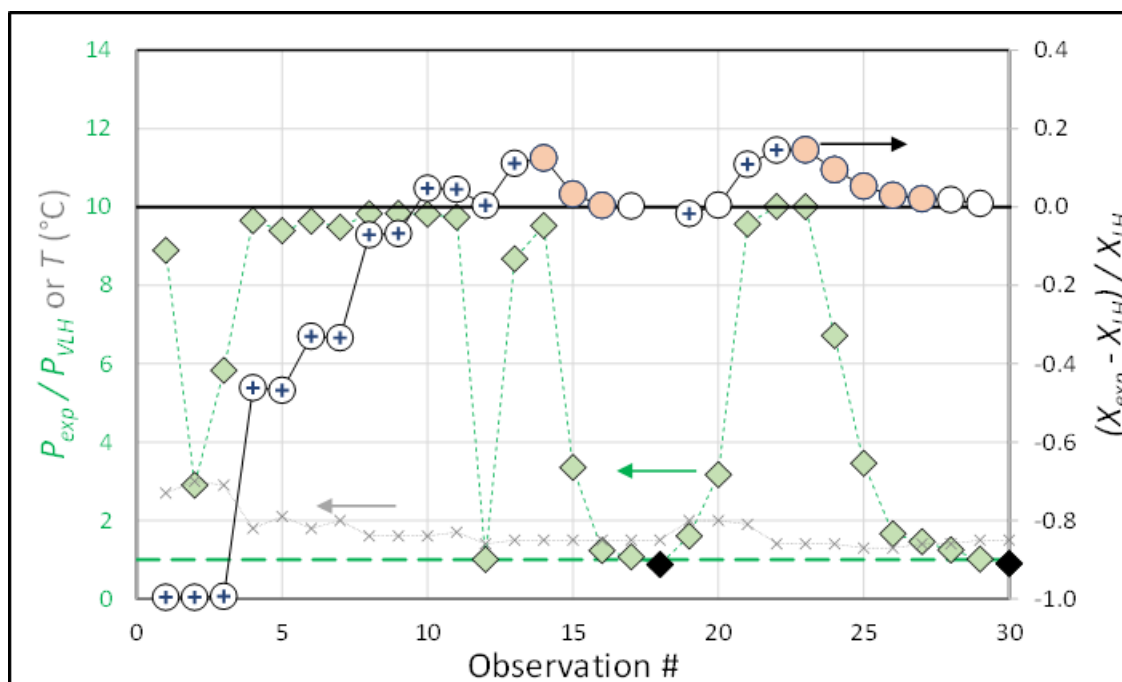


Figure 5. Graphical depiction of the 30 observations made on 16 CH₄ bubbles in RO water in the HWTF in Data Set A-5 (refer to Appendix A). The observations are chronological. The various symbols represent values at an individual bubble observation or an event, such as gas exsolution and/or system heating to attempt to eliminate any hydrate memory effect.

Circles: Values of $(X_{exp} - X_{LH})/X_{LH}$, which represent the fraction experimental dissolved gas saturation relative to the LH equilibrium value. A value of -1.0 indicates no dissolved gas with 0.0 indicating that the dissolved gas level is at the predicted value of LH ($X_{exp} = X_{LH}$). Values > 0.0 indicate supersaturation.

Open circles: no hydrate.

Orange-filled circles: hydrate.

Plus (+) in circle: new bubble injected into the HWTF bubble cup and released for observation.

Black horizontal line: $(X_{exp} - X_{LH})/X_{LH} = 0$ (right Y axis). Positive values indicate the system is supersaturated in dissolved CH₄ with respect to predicted LH equilibrium concentration.

Diamonds: Values of P_{exp}/P_{VLH} , which is the ratio of the average experimental pressure to the VLH pressure at the average temperature of the observation (left Y axis).

Green Diamonds: Bubble observations.

Black diamonds: Gas exsolution, which involves lowering the system pressure until dissolved gas comes out of solution.

Green dashed horizontal line: $P_{exp}/P_{VLH} = 1$ (left Y axis) indicating when the system pressure is at the VLH pressure.

Grey x: Average experimental temperature of the observation (left Y axis).

All VLH and LH values are from the WVU thermodynamic model developed on this project and described later in this report.

Hydrate formed on two separate bubbles during the observations in Figure 5. In both cases initial formation occurred near 30 MPa. In both cases the pressure was reduced in steps to melt or decompose the hydrate (Observations #14 to #17 and #23 to #28 in Figure 5), which occurred as the VLH equilibrium pressure was approached ($P_{exp}/P_{VLH} \rightarrow 1$).

Hydrates did not form on bubbles until the system was supersaturated with respect to the calculated LH equilibrium. All but one of the observations in the supersaturated region were on single bubbles. The exception is Observation #12 in which 12 smaller bubbles (~3 mm diameter) inadvertently came into the unit as the system pressure was reduced prior to the next bubble injection. No hydrate formed on this small swarm of bubbles; however, hydrate did form on the next larger bubble after its release from the HWTF bubble cup and while pressure was being increased in the range of from 20 to 29 MPa.

The data sets in Appendix A also all contain similar graphs, comments and notes that explain any atypical events or observations.

Overview of C1C2C3 data

Table 3 contains a summary of individual bubble observations for C1C2C3 in RO water. The observations were all made at a simulated depth of 3000 m (30 MPa).

Table 3. Summary of individual C1C2C3 bubble observations in RO water in the HWTF.

T, °C	1 to 3		4 to 6		7 to 9		10 to 13	
X_{C1C2C3}	0 to 0.000508		-		0.000348 to 0.000710		0.000698 to 0.000702	
Depth, m (psia) ↓	NH	H	NH	H	NH	H	NH	H
<500 (<740)	-	-	-	-	-	-	-	-
500-650 (740-957)	-	-	-	-	-	-	-	-
650-750 (957-1102)	-	-	-	-	-	-	-	-
750-1000 (1102-1465)	-	-	-	-	-	-	-	-
1000 (1465)	-	-	-	-	-	-	-	-
1500 (2190)	-	-	-	-	-	-	-	-
2000 (2915)	-	-	-	-	-	-	-	-
2500 (3641)	-	-	-	-	-	-	-	-
3000 (4366)	9	2	0	0	14	3	2	0
Total bubbles	9	2	0	0	14	3	2	0

Table Notes

- X_{C1C2C3} : Mole fraction of C1C2C3 dissolved in the water (prepared by reverse osmosis) in the HWTF.
- NH and H: No Hydrate formed and Hydrate formed, respectively. The numbers below these headings represent the number of individual bubbles injected and observed.
- The conditions in the table represent initial conditions.
- 30 individual bubbles were injected and released into the HWTF.
- 25 individual bubbles were hydrate free during observation.
- 5 bubbles formed hydrate during or after injection.
- 8 cycles were performed to melt hydrate by stepwise depressurization.
- 4 cycles were performed to form hydrate by stepwise pressurization.

Experiments with the C1C2C3 gas mixture were performed during three different time periods. The set of bubble observations in RO water (Table 3) were performed from 11/13/2012 to 1/31/2013 for comparison to the previous observations with methane. This was followed by

bubble observations in 35 salinity artificial seawater prepared from Instant Ocean®. The first observations were made during the time periods of 2/8/2013 to 3/21/2013 and 5/20/2013 to 6/28/2013. A second batch of seawater was made and another set of observations performed from 11/7/2013 to 11/21/2013. A final set of bubble observations were made with 200 ppm COREXIT 9500 added to the seawater from 1/30/2014 through 3/21/2014.

Table 4 summarizes individual bubble observations for C1C2C3 in 35 salinity artificial seawater. This was the largest set of measurements with observations performed at various pressures.

Table 4. Summary of individual C1C2C3 bubble observations in 35 salinity artificial seawater (Instant Ocean®) in the HWTF.

T, °C	1 to 3		4 to 6		7 to 9		10 to 13	
X_{C1C2C3}	0 to 0.00459		0.000455		0 to 0.000623		0 to 0.000870	
Depth, m (psia) ↓	NH	H	NH	H	NH	H	NH	H
<500 (<740)	-	-	-	-	1	-	1	1
500-650 (740-957)	-	-	-	-	-	-	2	-
650-750 (957-1102)	-	-	-	-	-	-	1	-
750-1000 (1102-1465)	-	-	-	-	-	-	-	-
1000 (1465)	4	3	-	1	8	2	18	4
1500 (2190)	-	-	-	-	-	-	-	-
2000 (2915)	4	-	-	-	6	1	14	1
2500 (3641)	-	-	-	-	-	-	-	-
3000 (4366)	15	3	-	-	8	2	15	3
Total bubbles	23	6	0	1	23	5	51	9

Table Notes

- X_{C1C2C3}: Mole fraction of C1C2C3 dissolved in the artificial seawater in the HWTF.
- NH and H: No Hydrate formed and Hydrate formed, respectively. The numbers below these headings represent the number of individual bubbles injected and observed.
- The conditions in the table represent initial conditions.
- 118 individual bubbles were injected and released into the HWTF.
- 97 individual bubbles were hydrate free during observation.
- 21 bubbles formed hydrate during or after injection.
- 20 cycles were performed to melt hydrate by stepwise depressurization.
- 5 cycles were performed to form hydrate by stepwise pressurization.

Table 5 summarizes a set of individual bubble observations for C1C2C3 in 35 salinity artificial seawater with the addition of 200 ppm COREXIT EC9500. Most of these observations were performed at 1 to 3°C and at a simulated depth of 3000 m (30 MPa).

In total, 193 individual bubble observations were made with C1C2C3. Of these, 154 bubbles were hydrate free during observation and 39 formed hydrate.

Figure 6 displays one of the data sets for C1C2C3 in a manner similar to Figure 5 for CH4. Unlike the observations in Figure 5, these observations became more complex near the end. This experimental sequence involved individual bubble observations at different pressures first in the range of 2 to 3°C and then at 6 to 7°C. The dissolved gas concentration was increased

progressively in steps to promote hydrate formation. Gas was added after Observations #3, #4, #6, #8, #19, and #21.

Table 5. Summary of individual C1C2C3 bubble observations in the HWTF in 35 salinity artificial seawater (Instant Ocean®) with 200 ppm COREXIT.

T, °C	1 to 3		4 to 6		7 to 9		10 to 13	
X_{C1C2C3}	0 to 0.00501		0.000456		0.000455 to 0.000623		0.000480 to 0.000482	
Depth, m (psia) ↓	NH	H	NH	H	NH	H	NH	H
<500 (<740)	1	-	-	-	-	-	-	-
500-650 (740-957)	-	-	-	-	-	-	-	-
650-750 (957-1102)	-	-	-	-	-	-	-	-
750-1000 (1102-1465)	-	-	-	-	-	-	-	-
1000 (1465)	1	2	1	-	-	1	-	-
1500 (2190)	1	-	-	-	-	-	-	-
2000 (2915)	-	2	-	-	-	1	-	-
2500 (3641)	-	-	-	-	-	-	-	-
3000 (4366)	24	4	-	-	2	3	2	-
Total bubbles	27	8	1	0	2	5	2	0

Table Notes

- X_{C1C2C3}: Mole fraction of C1C2C3 dissolved in the artificial seawater in the HWTF.
- NH and H: No Hydrate formed and Hydrate formed, respectively. The numbers below these headings represent the number of individual bubbles injected and observed.
- The conditions in the table represent initial conditions.
- 45 individual bubbles were injected and released into the HWTF.
- 32 individual bubbles were hydrate free during observation.
- 13 bubbles formed hydrate during or after injection.
- 14 cycles were performed to melt hydrate by stepwise depressurization.
- 3 cycles were performed to form hydrate by stepwise pressurization.

In this data set hydrate formed on 3 bubbles. The first occurrence was on the tenth bubble, represented by Observations #10 (no hydrate) and #11 (hydrate). Depressurization steps (#12 to #16) were carried out to observed hydrate decomposition. Even at the lowest pressure at #16 (2.186 MPa) hydrate had diminished but still was present.

The next bubble (Observation #17) was injected after the temperature had been raised to 6.3°C to see if raising the temperature would eliminate any hydrate memory effect. This bubble was observed at 30.00 MPa for 39 minutes without hydrate formation. However, during pressure reduction to ~3.7 MPa and mixing the HWTF by flow reversal, a small piece of hydrate was noted. The next step (#18) was further reduction in pressure to exsolve gas in an attempt to eliminate any hydrate memory effect.

The next bubble (Observation #s 19) did not form hydrate during 45 minutes of observation indicating that gas exsolution appeared to eliminate a memory effect that heating had not completely accomplished. The dissolved gas content was then increased as evidenced by the

increase in $(X_{exp} - X_{LH})/X_{LH}$ between #19 and #20 in Figure 6. The next two bubbles (#20 and #21) also did not form hydrate during observation lasting 42 and 60 min, respectively.

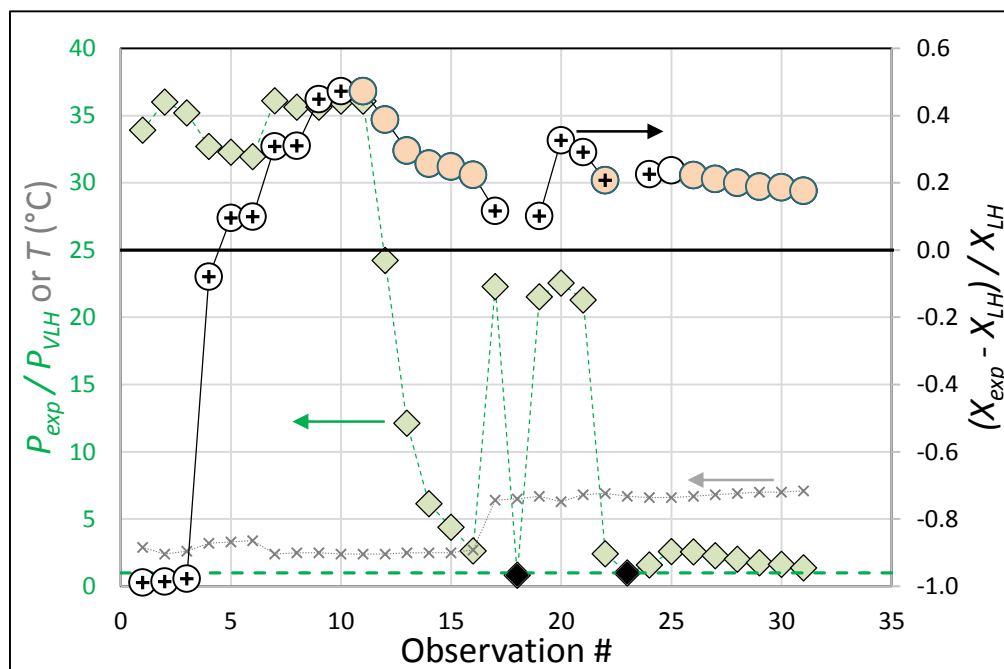


Figure 6. Graphical depiction of the 32 observations made on 16 individual C1C2C3 bubbles in RO water in the HWTF in Data Set B-2 in Appendix B. The observations are chronological. The various symbols are defined in the caption to Figure 5.

Additional gas then was added to elevate the dissolved gas level in the HWTF prior to another bubble observation. The same conditions of gas flow rate into the HWTF (5 ml/min) and pressure (~3.4 MPa) were used as in the prior five gas additions in this data set. Likewise water downflow was used to maintain the swarm of bubbles in the viewing region of the HWTF.

Hydrate formed on bubbles in the swarm after about 6 minutes of gas addition, which lasted 7 minutes. This observation is indicated as #22 in Figure 6. The value of $(X_{exp} - X_{LH})/X_{LH}$ is lower owing to the fact that the gas addition was performed at a pressure close to the VLH pressure (#22 in Figure 6).

Gas exsolution (black diamond at #23) was then performed to decompose the hydrate at a $P_{exp}/P_{VLH} = 0.98$, just below the VLH. The pressure was then slowly increased over 98 minutes to 3.48 MPa to dissolve the added gas into the water, which would be at $X_{C1C2C3} = 0.000679$ mol fraction when completely dissolved. No hydrate was observed on undissolved bubbles as the pressure was increased (#24 and #25 in Figure 6). After a few minutes the water flow was increased and a larger hydrated bubble came into view that was reasonably stable (#26 in Figure 6). Pressure was slowly reduced until no hydrate was observed on the remaining bubbles in the HWTF (#27 through #32). This larger, hydrated bubble likely formed from added gas that had accumulated and coalesced in the top of the HWTF viewing section. This experimental series was ended after reducing pressure to decompose the hydrate on this bubble.

All of the data sets in Appendix B contain similar graphs, comments and notes that explain atypical events or observations. In most of these data sets, more extensive heating, sometimes with gas exsolution, was used in attempts to eliminate any hydrate memory effect. The presence of ethane and especially propane in the C1C2C3 mixture likely make memory effects more difficult to eliminate.

Effect of gas saturation on initial hydrate formation

It is evident from Figures 5 and 6 above and other similar figures in Appendices A and B that the initial formation of hydrate on a gas bubble in the absence of any hydrate memory effect requires an elevated dissolved gas concentration. Figure 7 summarizes these observations for CH₄ in terms of both (a) the actual supersaturation of dissolved gas, expressed as mole fraction, and (b) the relative supersaturation. The symbols represent the first bubble in a data set that formed hydrate as the dissolved gas concentration was increased incrementally at a simulated depth of 3000 m (30 MPa). The incremental increase in dissolved gas concentration from the last hydrate-free bubble at the same pressure was approximately 0.00007 mol fraction for CH₄ and from 0.00001 to 0.00005 mol fraction for C1C2C3. All X_{LH} values in this and subsequent figures were obtained from the WVU thermodynamic model developed on this project, which is described later in this report.

It is evident from Figure 7a that there is a positive correlation between the actual supersaturation needed for initial hydrate formation and water temperature for both gases at this pressure level in either fresh or seawater. The rate of increase is less for C1C2C3. Seawater lowers the amount of supersaturation needed for either gas; however, the rate of increase appears to be independent of salinity. The same trends are evident on a relative basis (Figure 7b) except for C1C2C3 in fresh water; however, only two data points were obtained in this case. Additional experiments are needed to validate these trends and to determine the effect of pressure on hydrate formation.

Effect of gas saturation on bubble dissolution

The relative dissolved gas saturation compared to equilibrium is the primary driving force for bubble dissolution. Other independent variables that influence dissolution include pressure, temperature, salinity, and in the case of engineered bubble plumes, such as mitigation strategies for an oil spill, the addition of dispersant. Dependent variables include conditions on the bubble surface (the gas/water interface) and the presence of surficial bubble hydrate.

Dissolution data are also contained in Appendices A and B for observations when a bubble was in view for sufficient time to make this determination. Additional details related to the dissolution data contained in these appendices are included in Appendix C.

The dissolution rate determination procedure is described in Warzinski, *et al.* (2014). Bubble dissolution (i.e., shrinkage) rates are reported as the rate of change in equivalent spherical radius, R_e . The bubble is treated as an oblate spheroid for which $R_e = \sqrt[3]{a^2b}$, where a is the major radius and b is the minor radius, and the major radius is assumed symmetric about the minor axis. Time-averaged bubble size and shape were determined based on averaging the two-dimensional bubble edge location using a moving set of 100 sequential high-definition (30 fps) video frames that fully image the bubble.

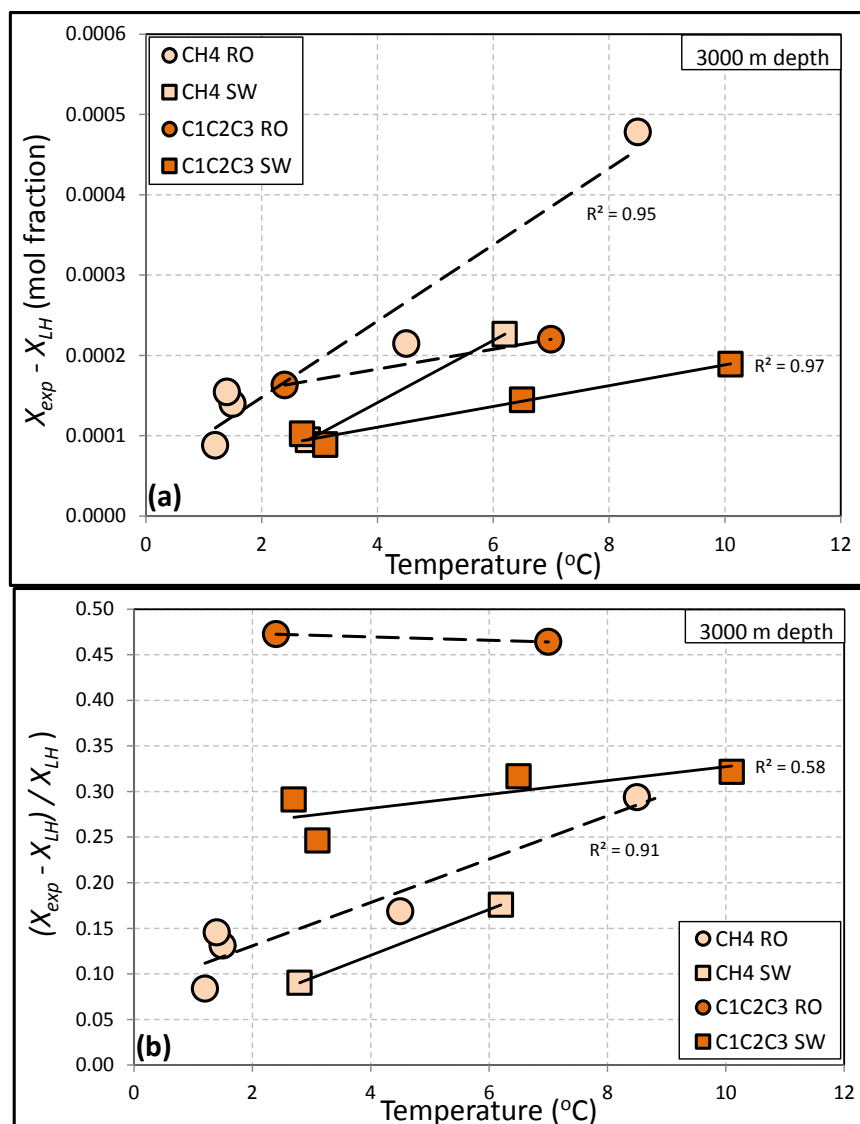


Figure 7. Dissolved gas supersaturation required for initial hydrate formation on bubbles of CH₄ and C1C2C3 in RO water and seawater (SW) as a function of temperature at a simulated depth of 3000 m. Values expressed as (a) absolute and (b) relative supersaturation.

A summary of the dissolution rates for hydrate-free bubbles are shown in Figures 8 and 9 for CH₄ and C1C2C3, respectively. Dissolution of hydrate covered bubbles is discussed in a later section on the effects of hydrate. The dissolution rate results are plotted as function of the relative supersaturation.

The data in Figures 8 and 9 show the expected behavior for light hydrocarbon gas bubble dissolution. The dissolution decreases with increasing dissolved gas level (equilibration) and pressure (the bubble gas is more dense). The variability with temperature is less and is not specifically identified in these figures.

The one difference between the pure CH₄ and the C1C2C3 mixture is that the former dissolution rates converge as expected as $X_{exp} \rightarrow X_{LH}$, whereas they do not for C1C2C3. This is likely due to

the change in bubble gas composition with time as methane and ethane preferentially dissolve faster in water than propane.

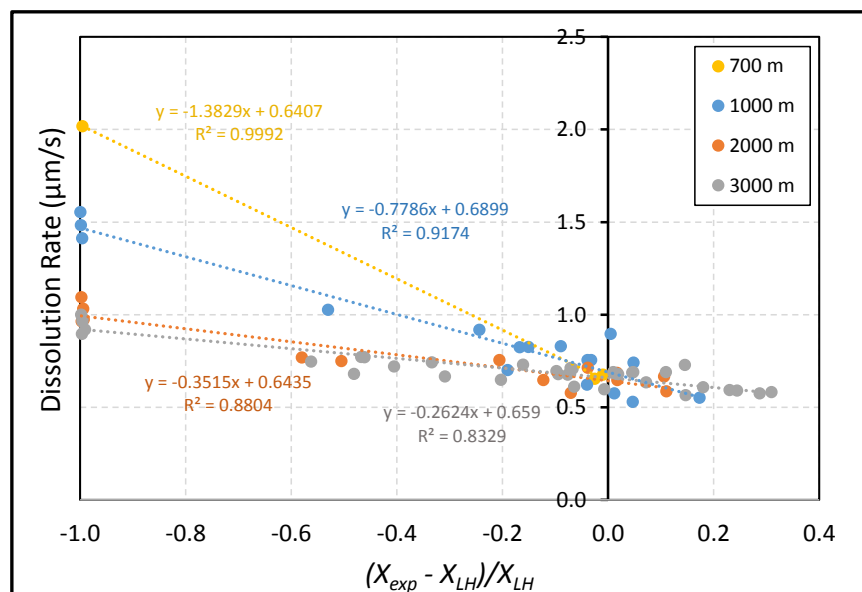


Figure 8. Dissolution rate ($\mu\text{m/s}$) for hydrate-free CH_4 bubbles observed in RO water in the HWTF as a function of the relative super-saturation, $(X_{\text{exp}} - X_{\text{LH}})/X_{\text{LH}}$ at simulated depths from 700 to 3000 m. Temperatures were varied from 1 to 13°C ; however, they are not specifically identified in this figure.

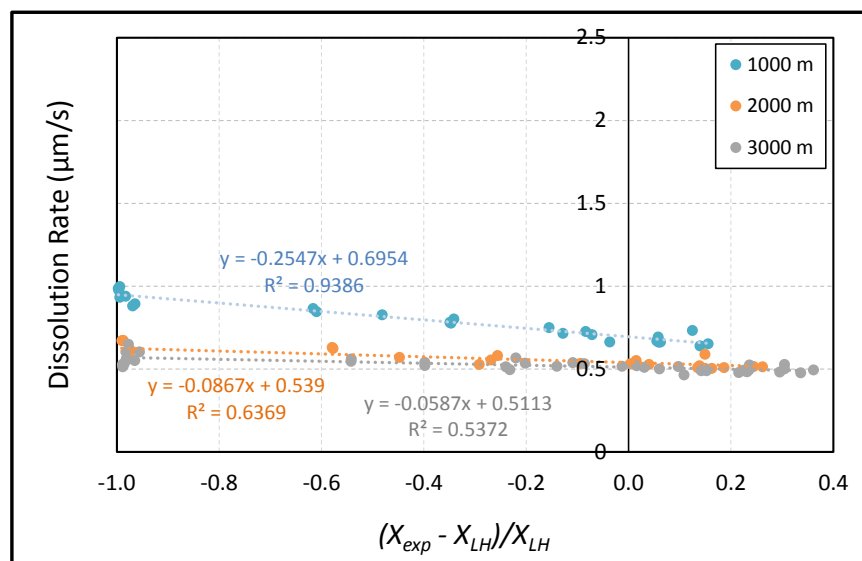


Figure 9. Dissolution rate ($\mu\text{m/s}$) for hydrate-free C1C2C3 bubbles observed in seawater in the HWTF as a function of the relative super-saturation, $(X_{\text{exp}} - X_{\text{LH}})/X_{\text{LH}}$ at simulated depths from 1000 to 3000 m. Temperatures were varied from 1 to 13°C ; however, they are not specifically identified in this figure.

Effect of temperature on bubble dissolution

Figure 10 summarizes the dissolution of CH₄ bubbles as a function of temperature at three different pressures and dissolved gas concentrations (shown in the figure legend simply as X).

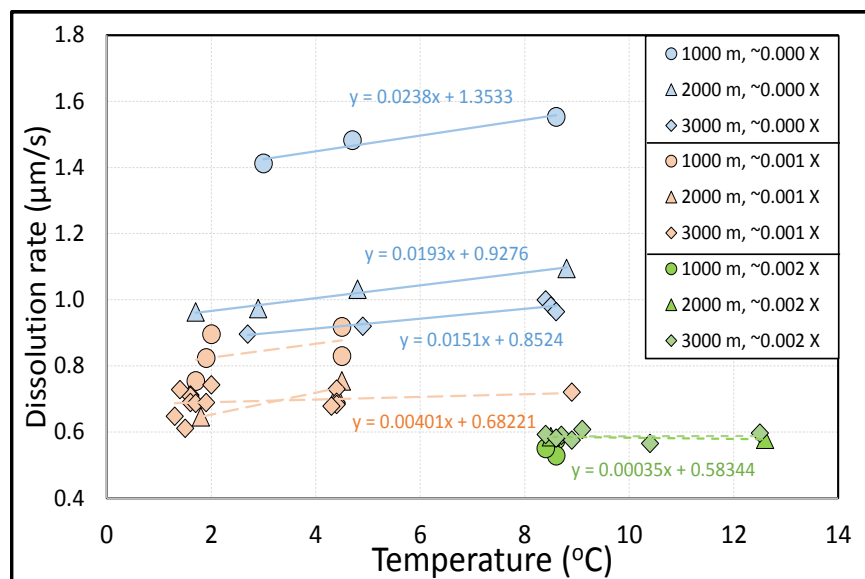


Figure 10. Dissolution rate (μm/s) for hydrate-free CH₄ bubbles observed in RO water in the HWTF as a function of temperature at three different levels of both simulated depth and dissolved gas concentration as indicated in the legend.

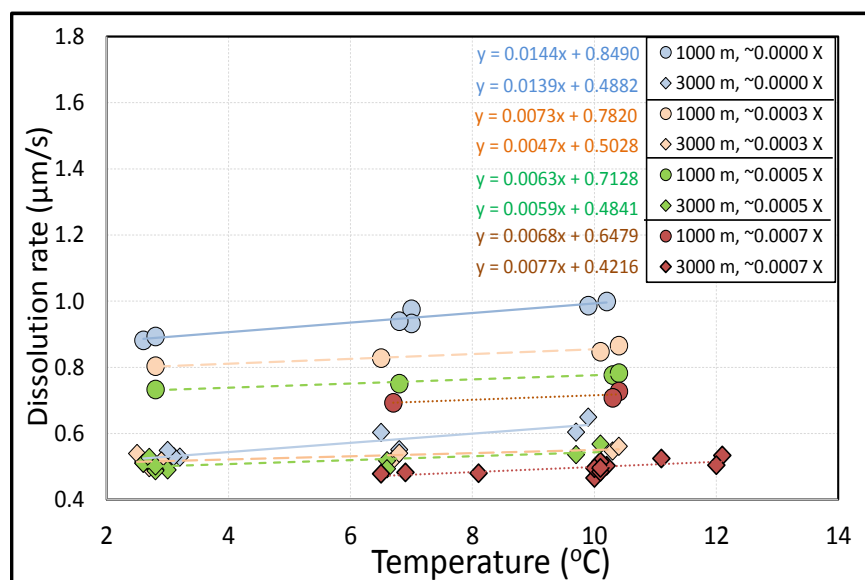


Figure 11. Dissolution rate (μm/s) for hydrate-free C1C2C3 bubbles observed in seawater in the HWTF as a function of temperature at two different levels of both simulated depth and four different levels of dissolved gas concentration as indicated in the legend.

Dissolved gas concentrations close to 0.0005 and 0.0015 mol fraction were not shown in Figure 10 to enable the trends to be more easily seen. Changes in pressure (simulated depth) are represented by different symbols; whereas changes in dissolved gas concentration are represented by color changes. These results provide a different perspective on the sensitivity of dissolution to these parameters than were discussed above for Figures 8 and 9 where temperature data were not treated separately. The effect of temperature is less than that of pressure and dissolved gas concentration, becoming almost negligible at the highest dissolved gas concentration shown where sufficient data were obtained for non-hydrated bubbles.

Figure 11 depicts similar results for C1C2C3 in seawater. The relative effects of dissolved gas concentration on dissolution are not as pronounced as compared to CH₄ in RO water in Figure 10, but are more comparable to the effects of pressure.

Effect of pressure on bubble dissolution

Figure 12 summarizes the dissolution of CH₄ bubbles in RO water as a function of pressure at different temperatures at three dissolved gas concentrations. Changes in temperature are represented by different symbols; whereas changes in dissolved gas concentration are represented by color changes. The effect of pressure or depth is greater at lower dissolved gas concentrations. As the dissolved gas concentration increases both pressure and temperature have less of an effect on dissolution.

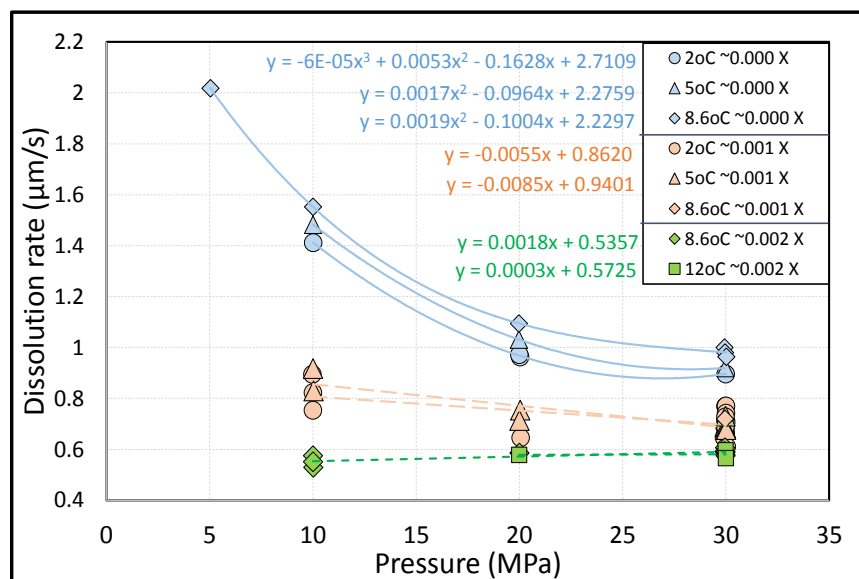


Figure 12. Dissolution rate (μm/s) for hydrate-free CH₄ bubbles observed in RO water in the HWTF as a function of pressure at different levels of temperature and dissolved gas concentration as indicated in the legend.

Figure 13 summarizes the dissolution of C1C2C3 bubbles in seawater as a function of pressure at different temperatures and dissolved gas concentrations. Changes in temperature are represented by different symbols whereas changes in dissolved gas concentration are represented by color changes. The axes are the same as in Figure 12 for comparison purposes. Similar to the results

for CH₄ in Figure 12, the effect of pressure or depth is greater at lower dissolved gas concentrations. Unlike the trends for CH₄ in Figure 12, pressure effects still are evident at the highest gas concentrations used before hydrate formation. As the dissolved gas concentration increases both pressure and temperature have less of an effect.

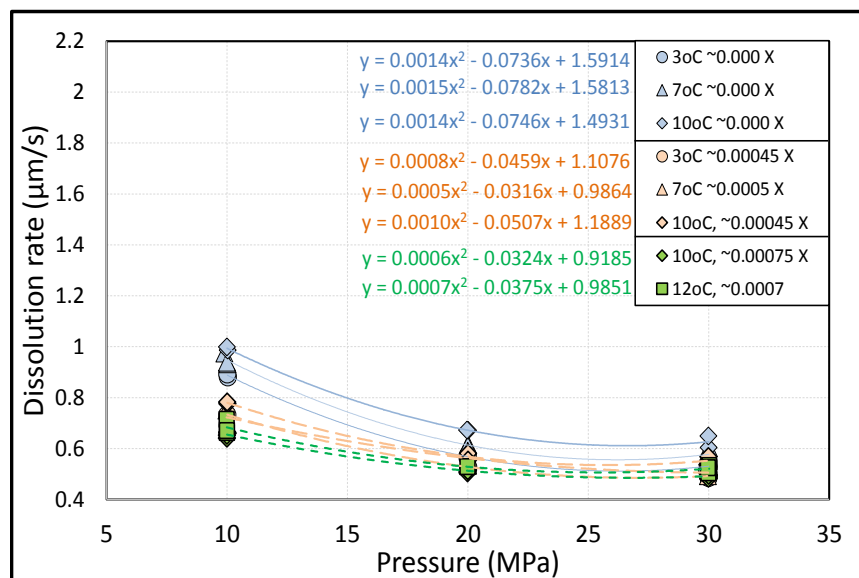


Figure 13. Dissolution rate ($\mu\text{m/s}$) for hydrate-free C1C2C3 bubbles observed in seawater in the HWTF as a function of pressure at four levels of temperature and three levels of dissolved gas concentration as indicated in the legend

Effect of salinity on bubble dissolution

As stated earlier in this report, more individual CH₄ bubble observations were performed in RO water than in the 35 salinity seawater (compare Tables 1 and 2). Enough experiments were performed in seawater to compare its effects on dissolution to the larger RO water data set. Figure 14 shows an overlay of the seawater data on the RO water data that were previously shown in Figure 8. The RO water data are low contrast colors to make the visual comparison easier. A molecular weight of 18.3 g/mol was used for the 35 salinity seawater in calculating X_{exp} .

The dissolution rates are lower in seawater; however, their relationships to the relative supersaturation levels are similar for data at the same simulated depths (pressures). The slopes of the 1000 and 3000 m seawater data are 3% higher and 10% lower, respectively, than in RO water. Only a limited number of CH₄ bubbles were observed in seawater at 2000 m; however, the relationship of dissolution rate to pressure is similar to that observed in the RO water.

The effect of seawater is similar for C1C2C3, as shown in Figure 15. The RO water experiments were performed to primarily investigate hydrate formation, thus most of the observations were at an $(X_{exp} - X_{LH})/X_{LH} > 0$. Based on the slopes of the linear regressions, the sensitivity of the dissolution rate to dissolved gas concentration is 35% lower in RO water than seawater.

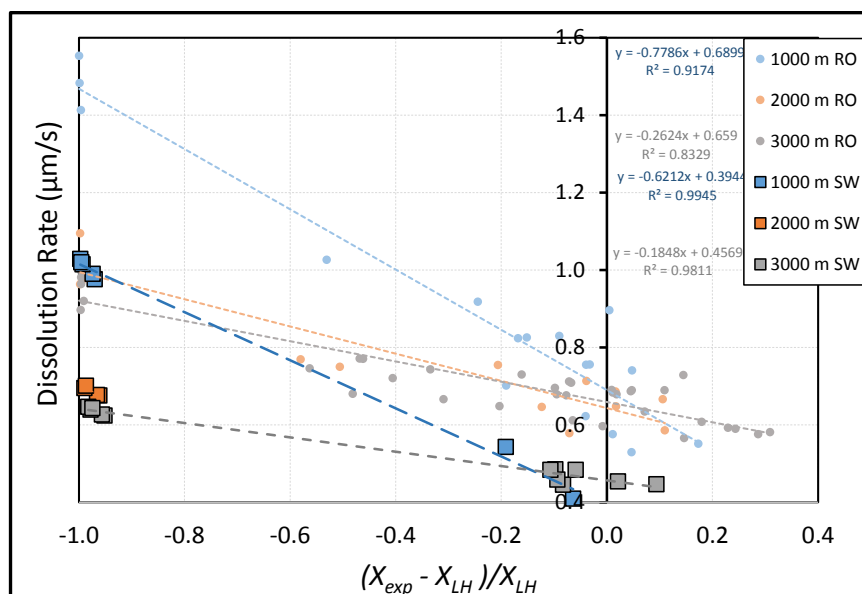


Figure 14. Dissolution rate ($\mu\text{m/s}$) for hydrate-free CH_4 bubbles observed in RO water and seawater in the HWTF as a function of relative supersaturation, $(X_{\text{exp}} - X_{\text{LH}})/X_{\text{LH}}$, at simulated depths from 1000 to 3000 m. Data from Figure 9 are shown for comparison. Temperatures were varied from 1 to 13°C in the RO water data and from 2 to 8°C in the seawater observations. The variations in temperature are not specifically identified in this figure. The linear correlation results are shown next to the legend for respective data at 1000 and 3000 m simulated depths.

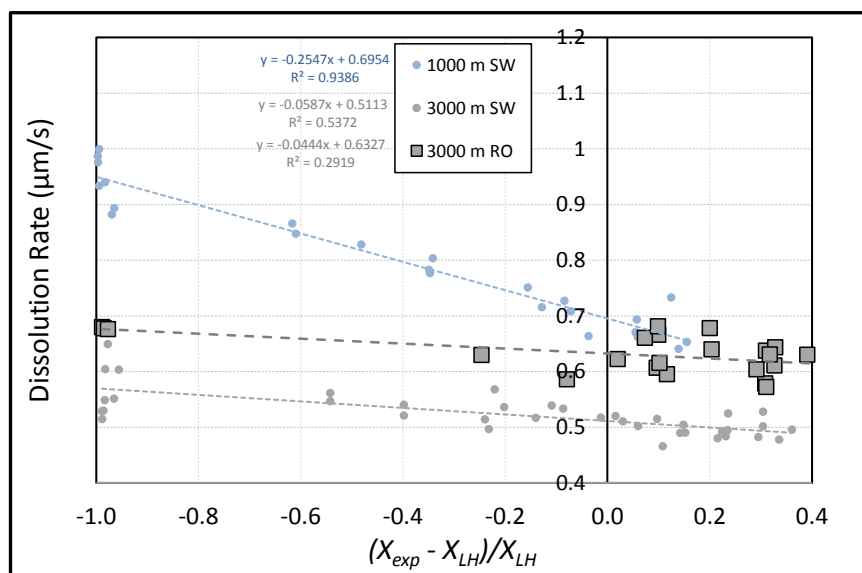


Figure 15. Dissolution rate ($\mu\text{m/s}$) for hydrate-free C1C2C3 bubbles observed in seawater and RO water in the HWTF as a function of relative supersaturation, $(X_{\text{exp}} - X_{\text{LH}})/X_{\text{LH}}$ at a simulated depth 3000 m. Data from Figure 9 are shown for comparison. At 3000 m, temperatures were varied from 3 to 11°C in the RO water data and from 2 to 12°C in the seawater observations. The variations in temperature are not specifically identified in this figure. The linear correlation results are shown next to the legend for respective data at 1000 and 3000 m simulated depth.

Effect of hydrate on bubble dissolution

The effect of hydrate formation on the dissolution rate of both CH₄ and C1C2C3 bubbles is shown in Figures 16a and 16b, respectively, and are referenced to the relative gas supersaturation. In both figures hydrated bubbles are represented by larger symbols with a black border and are indexed to simulated depth by color as shown in the legend. The “H” in the figure legends indicate hydrate formed. The prior dissolution data from Figures 8 and for non-hydrated CH₄ bubbles in RO water and C1C2C3 bubbles in seawater, respectively, are also shown for comparison.

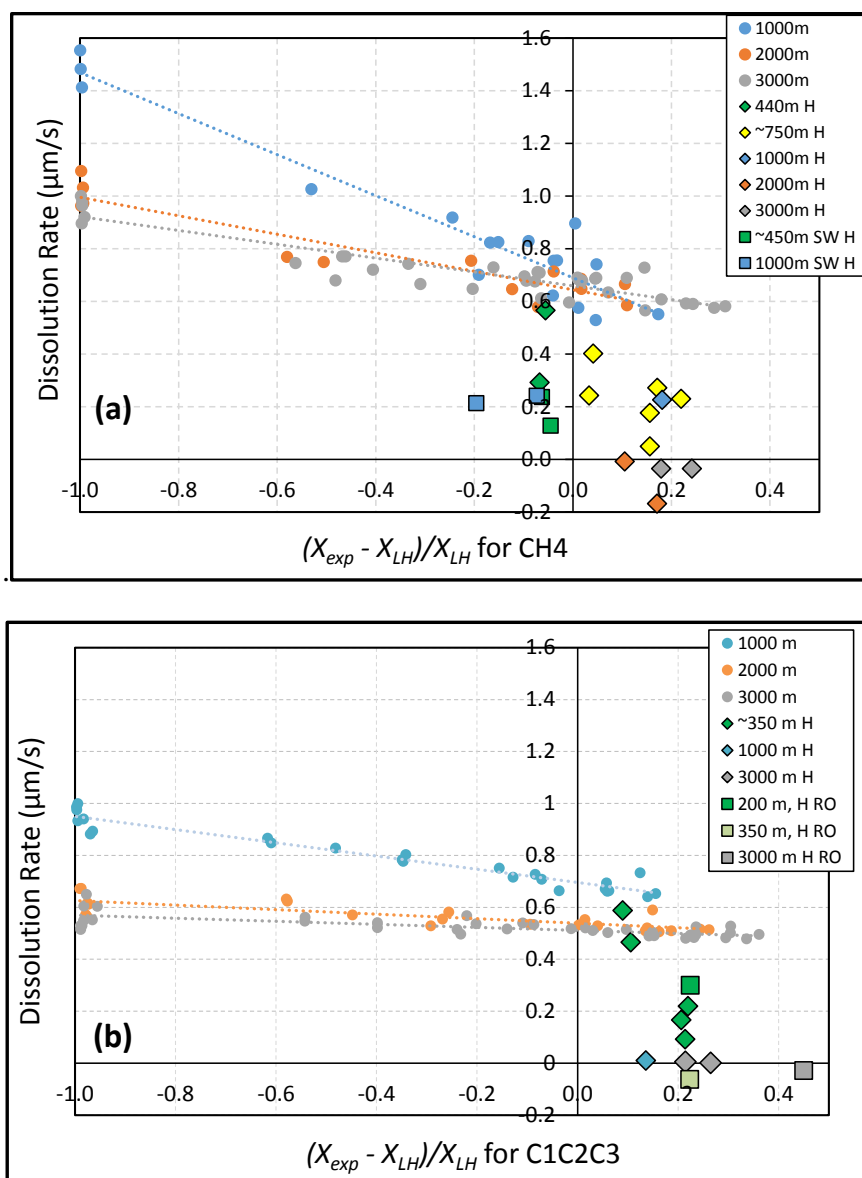


Figure 16. Comparison of the effect of hydrate formation on the dissolution rate of bubbles of (a) CH₄ and (b) C1C2C3. In (a) SW indicates seawater, no marking is RO water. In (b) RO is indicated, seawater is not. Hydrated bubbles in (a) and (b) are indicated in the legend by an H. The data are referenced to the relative gas saturation $(X_{exp} - X_{LH})/X_{LH}$.

The only seawater data shown (SW in legend) in Figure 16a are for CH₄ bubbles that formed hydrate. Similarly, the only RO water data shown (RO in legend) in Figure 16b are for C1C2C3 bubbles that formed hydrate.

While no clear trends are observed in the dissolution data for hydrate covered bubbles, most had dissolution rates that were markedly lower than for the respective hydrate-free bubbles. A general trend to lower dissolution rates is evident with increasing relative dissolved gas concentrations, but correlation to pressure, temperature, or salinity is not readily apparent. No size change and even growth of hydrated bubbles are also evidenced for both gases in these figures.

Figures 17 and 18 provide more detail on the relationship of dissolution rate to hydrate formation by showing only the data for hydrated bubbles. The relationship to temperature, pressure and salinity are more fully brought out and are indexed to symbol type and color as shown in the figure legends. Figure 17a and b depict these relationships for CH₄ and C1C2C3, respectively, as a function of the relative supersaturation, $(X_{exp} - X_{LH})/X_{LH}$.

For Figure 17a, other than the general decrease in dissolution rate with the relative level of dissolved gas, no other correlations are apparent in this data set.

However, for Figure 17b, there does appear to be a trend in the lower pressure (shallower depth) data as indicated in by the regression line, which only includes the seawater data at depths of 300 to 400 m.

Another factor that can bring more clarity to the question of when does a hydrated bubble experience significant dissolution as compared to very low dissolution or even slow growth is the comparison of the dissolution rates to the degree that the bubble is inside the VLH region, which is represented by P_{exp}/P_{VLH} . This is shown in Figures 18a and 18b for CH₄ and C1C2C3, respectively. The P_{VLH} data are from the WVU thermodynamic model described later in this report. The P_{exp}/P_{VLH} values for the C1C2C3 hydrated bubbles is larger than for CH₄ due to the lower VLH values at any given pressure (see Figures 25 and 26 below).

Except for one data point in Figure 17b (300 m, 7°C, in RO water) several observations are possible. For both gases, significant dissolution of bubbles with a hydrate skin is only observed at $P_{exp}/P_{VLH} < \sim 3$. Above this value, significant dissolution is not observed. No obvious correlations with hydrate growth are apparent. When growth is observed, the bubble either increases in size by continued hydrate crystallization from dissolved gas on the surface of the hydrated bubble or by simple accumulation of snow-like particles that have formed in the bulk aqueous phase. The latter case has been observed as strands or whiskers growing on the bubble surface.

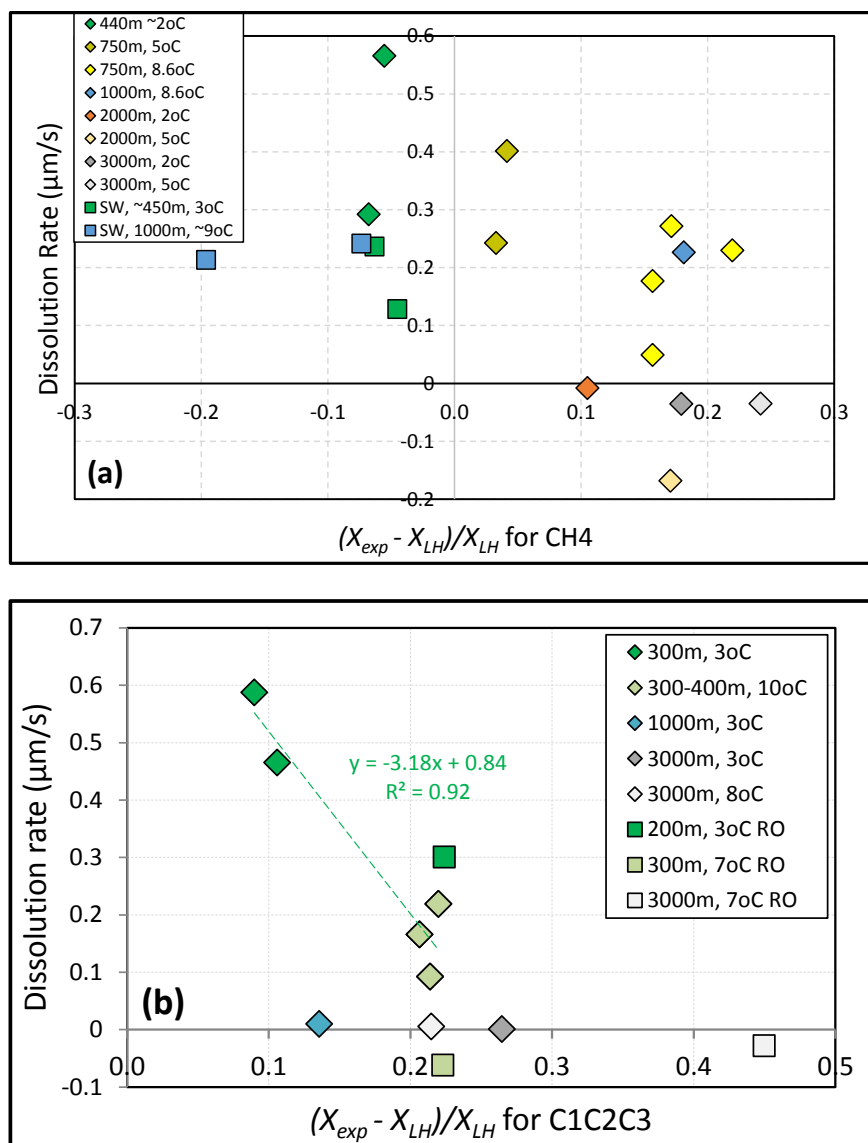


Figure 17. The effect relative gas saturation, $(X_{exp} - X_{LH})/X_{LH}$, on the dissolution rate of hydrated bubbles for (a) CH₄ in RO water and seawater and (b) C₁C₂C₃ in seawater and RO water.

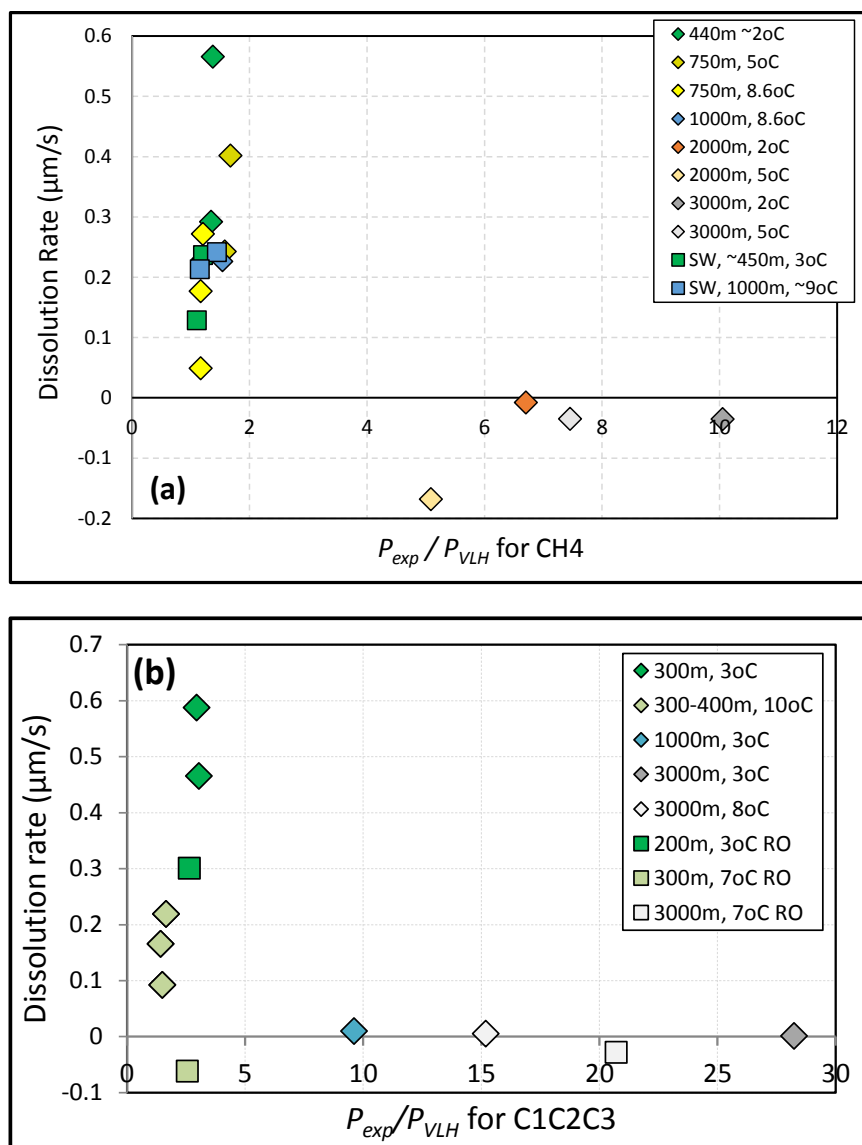


Figure 18. The effect how far the bubble is inside the VLH region, $P_{\text{exp}}/P_{\text{VLH}}$, on the dissolution rate of hydrated bubbles for (a) CH₄ in RO water and seawater and (b) C1C2C3 in seawater and RO water.

Effect of COREXIT EC9500 on bubble dissolution and hydrate formation

A final series of C1C2C3 bubbles were introduced into the HWTF that contained artificial seawater with 200 ppm COREXIT EC9500. A total of 45 individual bubbles were introduced; of which 13 formed hydrate. Figure 19 summarizes the results where dissolution rates could be obtained.

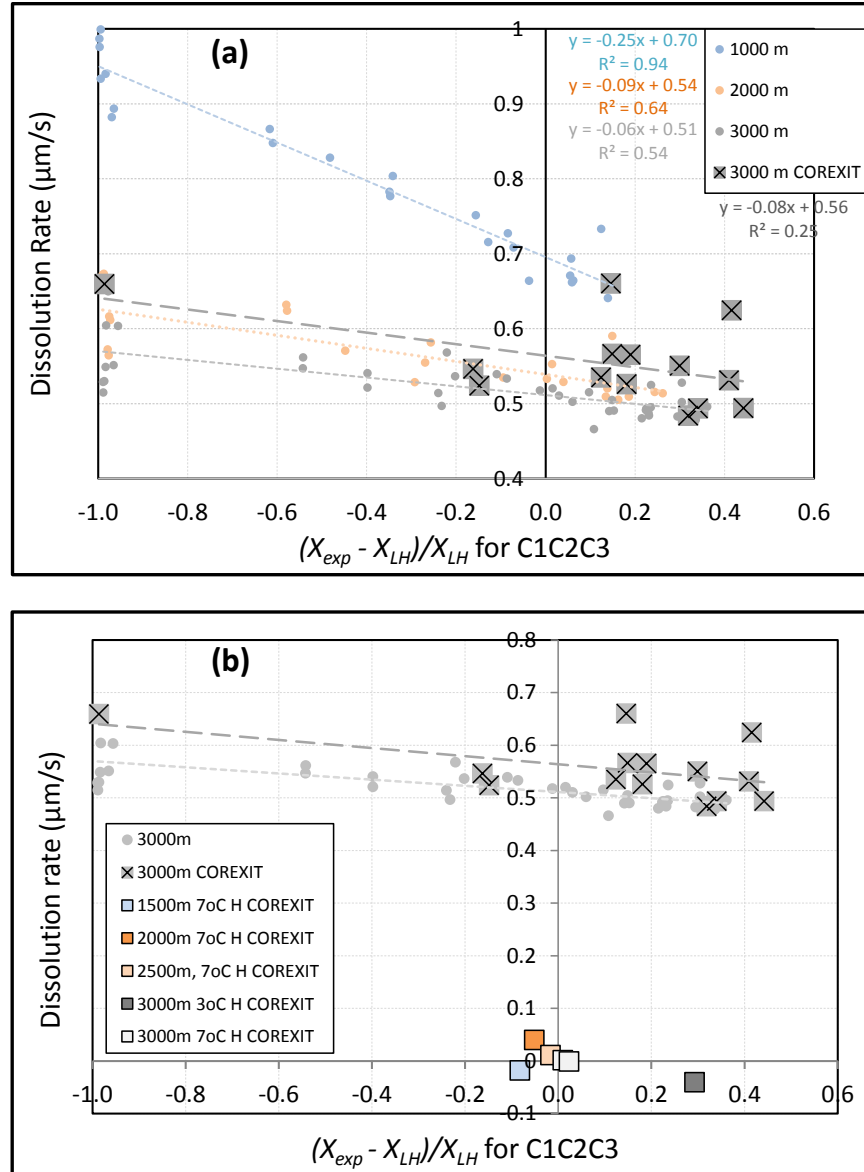


Figure 19. Comparison of the effect of COREXIT EC9500 on the dissolution rate of C1C2C3 bubbles in 35 salinity artificial seawater containing 200 ppm this dispersant. Dissolution rates of non-hydrated bubbles are shown in (a), which also compares these data, all obtained at a simulated depth of 3000m, to the C1C2C3 data in seawater without dispersant (Figure 9). Dissolution rates for bubbles with hydrate are shown in (b) where a comparison is only made to previous data without dispersant at 3000 m simulated depth. All data are compared as a function of relative gas saturation $(X_{exp} - X_{LH})/X_{LH}$.

Before discussing these results, the effect of the dispersant in general was to cause the ~1.5 cm bubble initially released into the HWTF to shear down to smaller sizes in almost all cases. Shearing varied, but typically from 1 to 5 shearing events occurred in the first few seconds to minutes. No bubbles less than ~3 mm diameter were observed, i.e., no very tiny (<1.0 mm) bubbles were observed. After the initial shearing events, 24 dissolution rates were obtained on 19 individual bubbles. Of these, 6 had formed hydrate shells, as shown in Figure 19b.

Figure 19a shows that the dissolution rate data, all obtained at 3000 m depth, were more scattered than the data without the dispersant. On average, the dispersant increased the average dissolution rate ~10% at the 3000 m depth investigated.

Figure 19b shows that all of the hydrated bubbles that were observed for periods long enough to obtain a dissolution rate had very low dissolution rates ($<0.4 \mu\text{m/s}$) or slow growth, even under subsaturated conditions. This is comparable to most hydrated bubbles previously observed at similar depths without the dispersant, as shown in Figure 18.

Effect of hydrate morphology on bubble dissolution

Considerable effort was invested in the latter part of this project on preparing and successfully publishing a manuscript entitled “Dynamic morphology of gas hydrate on a methane bubble in water: Observations and new insights for hydrate film models,” which was recently published in *Geophysical Research Letters* (Warzinski, *et al.*, 2014). The abstract reads:

“Predicting the fate of subsea hydrocarbon gases escaping into seawater is complicated by potential formation of hydrate on rising bubbles that can enhance their survival in the water column, allowing gas to reach shallower depths and the atmosphere. The precise nature and influence of hydrate coatings on bubble hydrodynamics and dissolution is largely unknown. Here we present high-definition, experimental observations of complex surficial mechanisms governing methane bubble hydrate formation and dissociation during transit of a simulated oceanic water column that reveal a temporal progression of deep-sea controlling mechanisms. Synergistic feedbacks between bubble hydrodynamics, hydrate morphology, and coverage characteristics were discovered. Morphological changes on the bubble surface appear analogous to macroscale, sea ice processes, presenting new mechanistic insights. An inverse linear relationship between hydrate coverage and bubble dissolution rate is indicated. Understanding and incorporating these phenomena into bubble and bubble plume models will be necessary to accurately predict global greenhouse gas budgets for warming ocean scenarios and hydrocarbon transport from anthropogenic or natural deep-sea eruptions.”

This paper and extensive supporting information provide a first ever look at phenomena that occur on the surface of a freely rising, hydrate coated bubble. Such phenomena and their dependence on bubble hydrodynamics were not previously postulated. A detailed description of the interactions between bubble hydrodynamics and hydrate morphological changes on the bubble surface and the impacts of these changes on rise velocity and bubble dissolution, two important parameters for subsea bubble and bubble plume modeling, have now been discerned.

Figure 20 contains the main figure and its caption from this manuscript.

The experiment in Figure 20 was performed in RO water at 8.8 to 8.9°C on a single CH₄ bubble that formed a hydrate shell as pressure was increased to 10.03 MPa as shown in bubble images a through d in Figure 20. A detailed high-definition video of the formation process (bubble images a to b) is available for viewing in the supporting information of the GRL paper. During this ~30 s video, the bubble oscillates freely with disconnected hydrate crystals forming on its surface until the crystals join to form an immobile shell or skin on the bubble. Such processes have been postulated but never seen at the level of detail in this experiment. The shift to an immobile interface resulted in a 6% decrease in rise velocity (see Figure 20 at ~500 s).

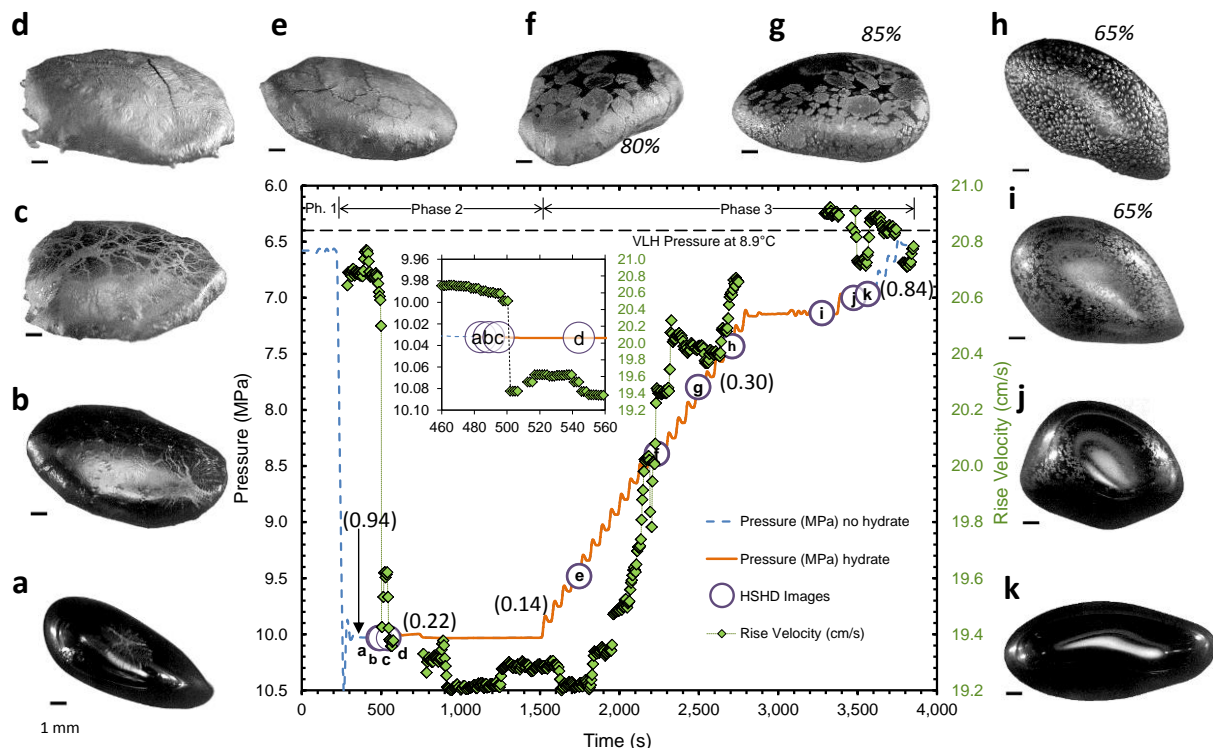


Figure 20. Observed hydrate morphology and rise velocity as a function of time, t , for a varying pressure cycle showing methane bubble hydrate shell formation and decomposition. At $t = 0$, the first of 68 small (~ 0.3 cm diameter) methane bubbles was introduced into a small inverted cup in the high-pressure water tunnel facility that rapidly coalesced to form a bubble of ~ 1 cm equivalent spherical diameter. The pressure scale is inverted to correspond to depth ($1\text{ MPa} \approx 100\text{ m}$ depth). The small inset chart expands the region of initial hydrate formation. Gaps in rise velocity, i.e., no dashed line indicate intervals when the bubble moved out of view. The black horizontal dashed line indicates the thermodynamic vapor/liquid/hydrate equilibrium pressure of 6.40 MPa at 8.9°C [Sloan and Koh, 2008]. The hydrate stability field is at pressures greater than this. Bubble images a – k correspond to experimental times noted by lettered circles on the pressure trace. Larger, high-resolution versions of these and additional images are in the supporting information of Warzinski *et al.* (2014). Shown below each image are 1 mm scale bars. Percentage of hydrate surface coverage is noted near Bubble images f, g, h, and i. Dissolution rate results are shown in parentheses. See Warzinski *et al.*, 2014 for details.

The hydrate covered bubble was held at the formation conditions for ~ 17 minutes, at which time the pressure was decreased in a stepwise manner to approximate natural decompression. These steps are shown in Figure 20 at times > 1500 s. Bubble images e through k were taken during decompression at the times shown on the pressure trace in Figure 20. Morphological changes in the hydrate were observed on the bubble surface that were not heretofore predicted and appear somewhat analogous to changes in surface sea ice. Transient cracks that were observed in the hydrate skin prior to decompression (bubble image d) became more pronounced on the bubble surface as decreasing pressure weakened the skin by both thermodynamic (hydrate dissolution)

and hydrodynamic (bubble expansion and increase in surface mobility processes). The increased surface motion fractured the surface into plates that moved about on the bubble surface, especially in the upper hemisphere. Water flow past the bubble pushed plates to the lower hemisphere where they were less affected by surface oscillations and likely more stable owing to a higher level of dissolved gas in the bubble wake. Continued depressurization resulted in surface mobility increasing with a concomitant increase in rise velocity, which for bubble images h, i, and j was near the rise velocity of the original hydrate-free bubble. The plates decreased in size owing to surface collisions (note the raised edges of the plates) and abrasion. They also thinned due to hydrate melting. The small plates finally covered most of the bubble surface and thinned until they were difficult to visually see (bubble image j). Bubble image k is hydrate free.

Hydrate surface coverage was estimated at times corresponding to bubble images f through i using a trainable segmentation technique that is described in detail in the supporting information of Warzinski *et al.* (2014). This supporting information also includes larger bubble images of those in Figure 20 and additional images taken between them. The dissolution rate methodology is also described in the supporting information along with the relationship between hydrate coverage and dissolution rate. Dissolution rates were determined prior to hydrate formation, with a hydrate shell during the constant pressure period at 1000 m, at the beginning of depressurization, during the interval when partial hydrate coverages were determined, and in the final hydrate-free state.

A link to an interactive Adobe Flash animation was also published in the supporting material in Warzinski *et al.* (2014). High-speed high-definition video clips of bubble images comparable to those shown in Figure 20 can be viewed in motion or studied frame by frame. The link is:

http://netl.doe.gov/hydrate/Hydrate_formation_&_melting_june29_2012.html

Figure 21 depicts the change in dissolution rate as a function of hydrate coverage. The first two dissolution rates were not used, owing to limited time for the first one with no hydrate coverage and for the second one where hydrate shedding was observed. A simple linear relationship is evident in this limited data set. While intuitively consistent with the assumption that bubble gas can freely escape through cracks and larger open areas on the bubble surface, this relationship is based on the limited data obtained to date and must be treated as preliminary and should not be used in bubble or bubble plume models until additional corroborating data are obtained.

An important observation on hydrate morphology that has arisen from this research is that the morphological features and their link to bubble surface hydrodynamics are similar to larger scale phenomena of sea ice. Figure 22 summarizes some of these similarities. The sea ice terms are in parentheses.

Effect of hydrate on rise velocity

Figure 20 illustrated a reduction in rise velocity as a result of hydrate formation on a bubble of CH₄. Experiments were also performed in which a stream of bubbles were injected directly into the HWTF (bubble cup turned to let bubbles pass by) at 14.5 MPa and 3°C with no water flow in

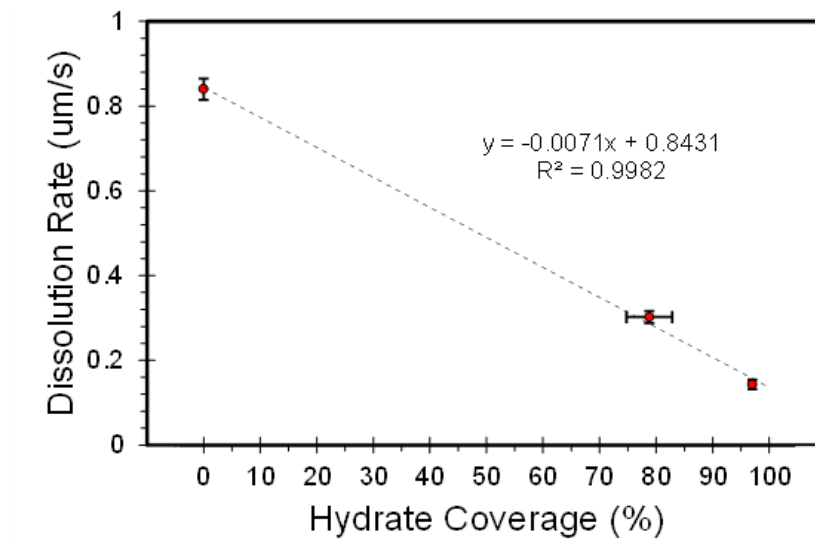


Figure 21. Relationship between dissolution rate, expressed as radial shrinkage rate, and hydrate coverage (HC). The HC at 79% is the time weighted averages of HC for five bubble images taken between 2235 s and 2693 s (refer to time scale in Figure 20). The vertical dissolution rate error bars represent the 95% confidence limits for these data. The horizontal error bars on the data at 79% HC represent the time-weighted standard deviations of experimental variability based on the averaging done to obtain this point.

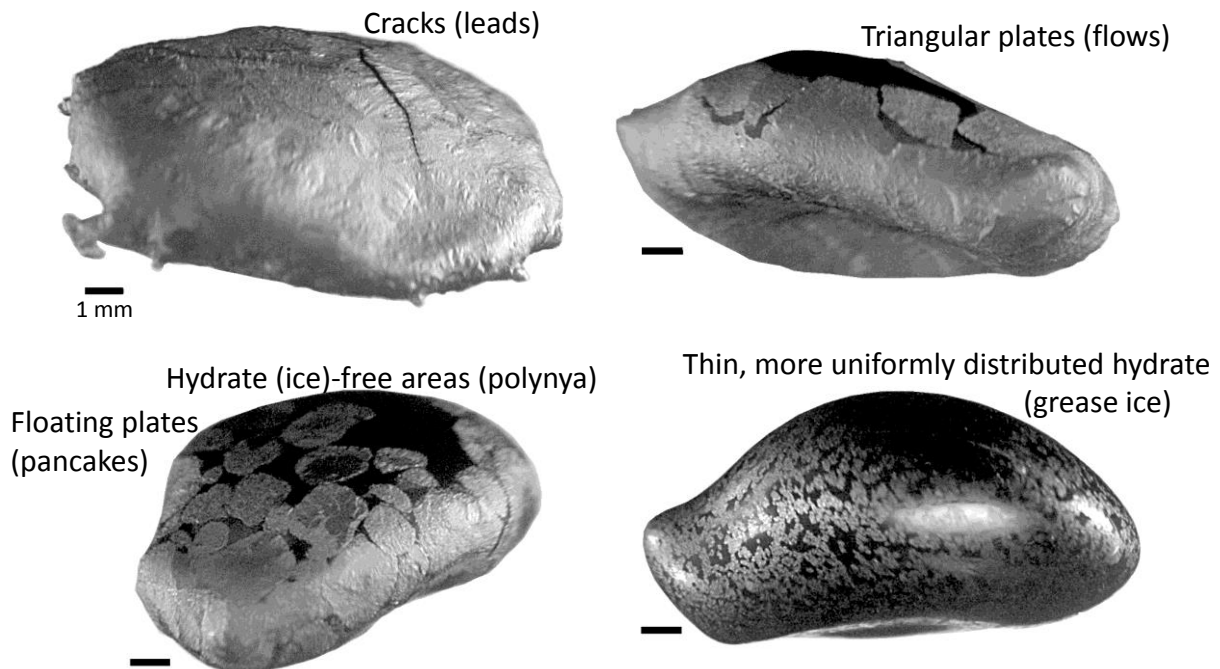


Figure 22. Enlarged bubble images from Figure 20 depicting features that are similar to those on larger scale (meters to kilometers) sea surface ice. Standard sea ice terms are shown in parentheses. For additional information see *Smith (2000)*.

order to determine the rise velocity of the bubbles using particle image velocimetry. The bubbles were injected at about 2 to 3 per second. No hydrate initially formed on the bubbles. Hydrate formed later in the observations as the dissolved gas concentration, which was not measured, increased. The results of the rise velocity measurements are shown in Figure 23. The velocity is plotted against Feret diameter, the longest diameter passing through the centroid of the bubble.

Bubbles of various sizes were able to be injected. Without hydrate, the bubbles fell into one of two regimes as shown in Figure 23. Small, nearly spherical, non-hydrated bubbles rose without oscillation with the rise velocity increasing as the injected bubble size increased. At about 1950 μm , the more ellipsoidal bubbles began to oscillate, causing a reduction in rise velocity as bubble size increased beyond this point.

Hydrate formation on small bubbles ($\sim < 1100 \mu\text{m}$) did not appear to affect rise velocity; however, as size increased, hydrate formation reduced the rise velocity for bubbles $> 1200 \mu\text{m}$. At 2100 μm the rise velocity was reduced by over 40%. Additional data in the 2000 to 3500 μm range was not attainable in the HWTF owing to bubble buoyancy on the injection tip (3.18 mm tubing). Based on the data in Figure 23, the lower rise velocities associated with hydrate formation would reduce the momentum in a bubble plume and cause bubbles to be dispersed over a wider range by ocean currents.

Bubble swarms and hydrate formation.

Small swarms of bubbles were introduced into the HWTF every time the dissolved gas concentration was increased. The bubbles were typically introduced into the HWTF viewing section at 3.45 MPa at a rate of 2 to 5 mL/min, with the lower flow rate used at higher dissolved gas concentrations. These flow rates introduced the bubbles as a steady stream of individual bubbles; no jet-type flows were used. A down flow of water or seawater was typically used to keep the bubbles in the viewing section while they dissolved. Allowing a swarm of gas bubbles to circulate in the flow loop (see Figures 2 and 3) can promote hydrate formation when the bubbles go through the high-pressure centrifugal pump (see Figure 3) owing to the shearing and mixing of the bubbles that could occur in this pump.

Figure 24 shows the $P_{\text{exp}}/P_{\text{VLH}}$ ratio as a function of temperature at 3.45 MPa for both CH₄ and C1C2C3 in both RO and seawater. For CH₄, gas additions above 3°C and 2°C were below the region of hydrate stability ($P_{\text{exp}}/P_{\text{VLH}} < 1$) for RO and seawater, respectively, and should not form hydrate upon injection except at or below these temperatures. On the other hand, injection of C1C2C3 at this same pressure may form hydrate during injection at temperatures up to 13°C and 14°C for injection into seawater and RO water respectively.

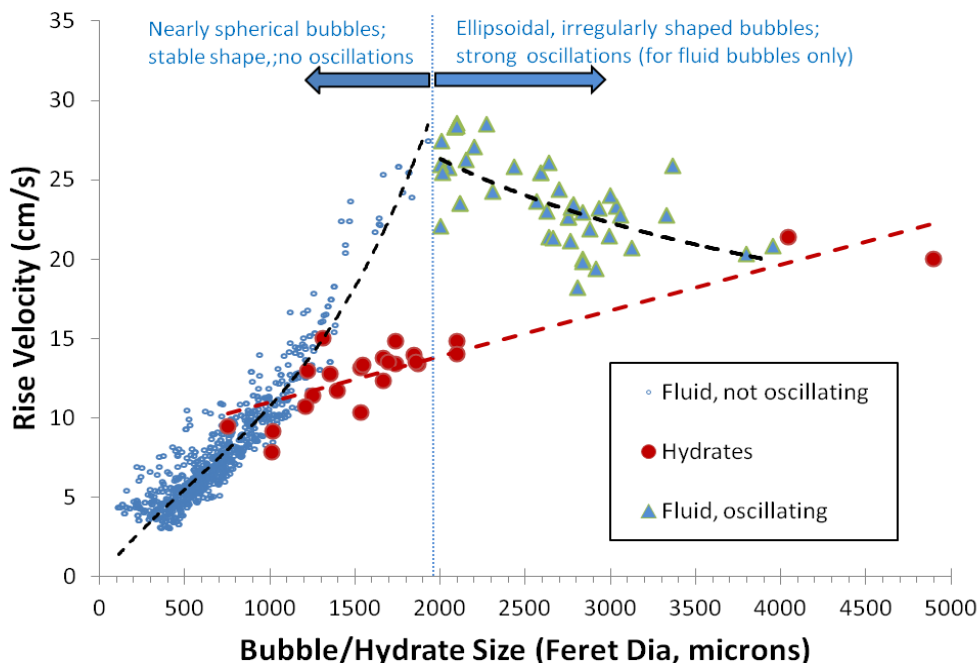


Figure 23. Rise velocity of C1C2C3 bubbles of various sizes released into the HWTF illustrating the effect of hydrate formation on rise velocity.

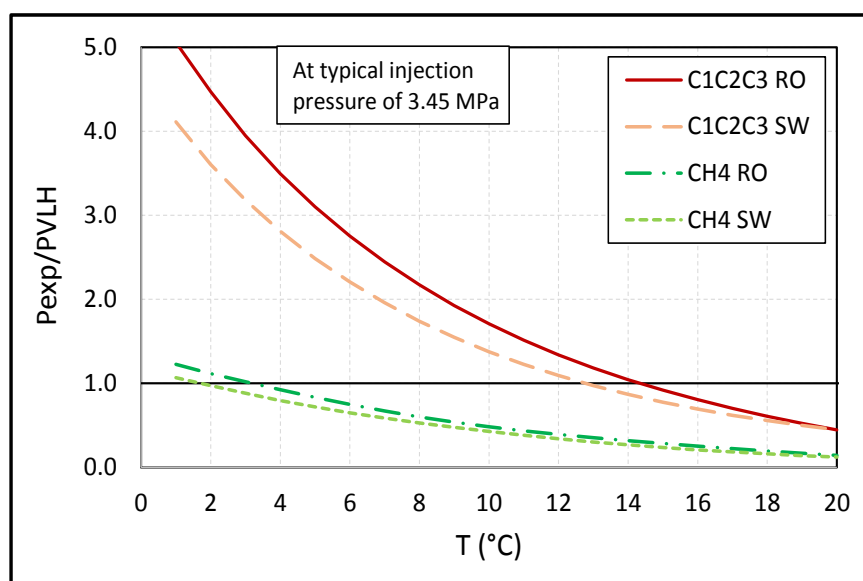


Figure 24. Typical gas injection conditions relative to VLH equilibrium for CH₄ and C1C2C3 in both RO water and seawater. Values above 1 on the abscissa indicate that hydrate is possible during the injection. Most injections to increase the dissolved gas content in the HWTF were performed close to 3.45 MPa.

Nearly all of the 44 CH₄ gas additions performed during the experiments summarized in Appendix A were performed with a $P_{exp}/P_{VLH} \leq 1.0$. Only five were at $P_{exp}/P_{VLH} > 1.0$, four at 1.2 and one at 6.5. In this latter case, the HWTF was at 19.995 MPa and 1.6°C, which promoted hydrate formation as CH₄ was being introduced at 0.7 ml/min. No hydrate formed at $P_{exp}/P_{VLH} = 1.2$. This is noted in Appendix A, Data Set 1, on 5/8/2012.

During C1C2C3 bubble observations, 50 gas additions were made to increase the level of dissolved gas in the HWTF. Only 4 of these injections were at $P_{exp}/P_{VLH} \leq 1.00$. The other 46 injections were in the range of 1.3 to 3.7. Out of these, three formed hydrate during the injection/dissolution process and were in the range of 2.4 to 3.7 and with relative saturation levels, $(X_{exp} - X_{LH})/X_{LH}$, near 0; i.e., near saturation $X_{exp} = X_{LH}$.

These results indicate that for slower seeps and leaks (no jet flow) hydrate is unlikely to form unless the dissolved gas concentration approaches LH equilibrium saturation.

Thermodynamic and Bubble Plume Modeling

Development of a thermodynamic model for sII hydrates

Understanding the fate and transport of hydrocarbons and hydrocarbon mixtures in the deep sea requires accurate determination of the two-phase liquid water (L) – hydrate (H) thermodynamic equilibrium in the absence of a free gas phase. In addition to controlling hydrate formation directly from the aqueous phase, the LH equilibrium provides the aqueous solubility of dissolving hydrate. The driving force for gas bubble dissolution with or without hydrate is the concentration difference between the hydrocarbon solubility at the interface and the bulk hydrocarbon concentration in the surrounding ocean. Accurate thermodynamic predictions of the solubility of hydrocarbon mixtures in seawater in the presence of hydrate therefore are necessary to model the dissolution rate of hydrate-covered bubbles as they transit the ocean water column. Both natural seeps and anthropogenic emissions can release hydrocarbon as well as pure methane gas bubbles. Therefore, bubble plume models require accurate thermodynamic predictions of nearly pure methane sI hydrates for biogenic seeps and mixed hydrocarbon sII hydrates for thermogenic seeps and anthropogenic releases.

For this project, Team members at West Virginia University (WVU) developed a thermodynamic model to calculate the aqueous solubility of hydrocarbon mixtures at LH equilibrium in fresh water or seawater. Complete details of the thermodynamic model are contained in a manuscript that is intended for submission to *Fluid Phase Equilibria*.

The model is based on the *van der Waals and Platteeuw* (1959) statistical thermodynamic model and the *Holder, et al.* (1980) model. Langmuir constants were calculated from cell potential parameters obtained from *ab initio* intermolecular potentials and thus the model contains no fitting parameters. The model accurately predicts the available experimental data for pure methane, ethane, and propane LH equilibrium solubility, including methane experimental data recently measured on this project.

The model also predicts hydrate phase molar concentrations for pure and mixed hydrocarbons, which are necessary for modeling hydrate phase and hydrate dissolution mass transport. Figures 25 and 26 show phase diagrams for CH₄ and C1C2C3 in seawater, respectively. This mixture

was chosen as a representative hydrocarbon mixture based on the methane-ethane-propane ratio from the 2010 Macondo oil spill and seepage from active sites in the Mississippi Canyon.

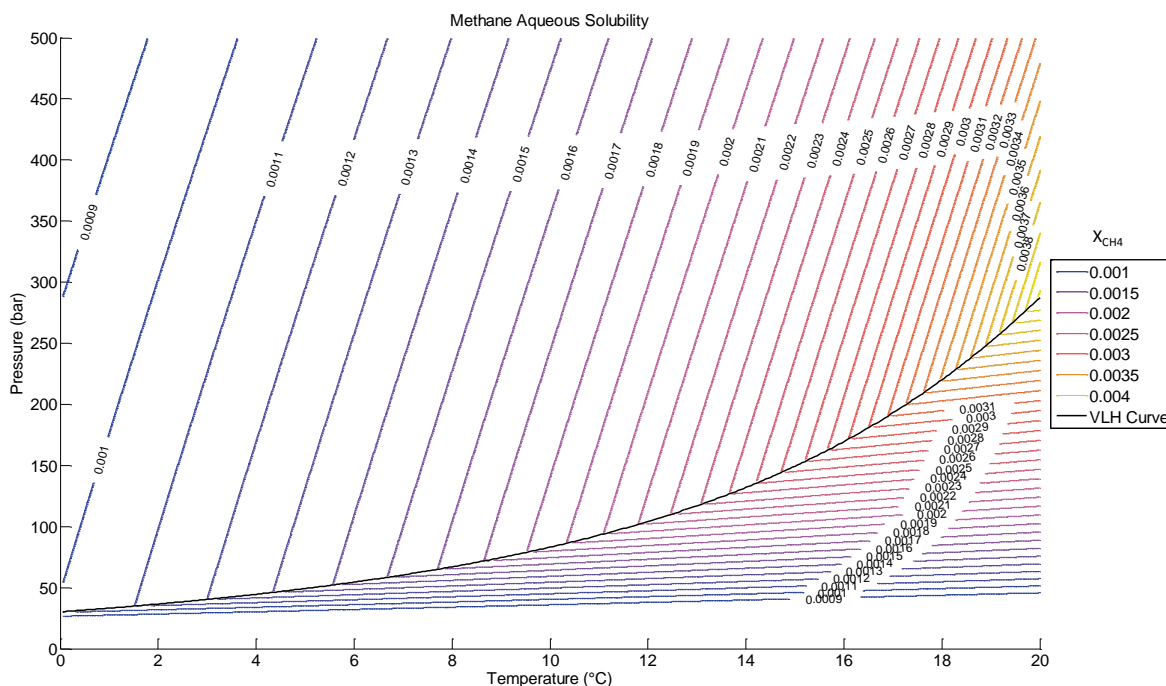


Figure 25. CH₄ in 35 salinity seawater phase diagram calculated with the WVU-NETL MATLAB model. The solid black line is the vapor-liquid water-hydrate (VLH) equilibrium curve, which is the lowest pressure/highest temperature at which hydrate is stable. The aqueous solubility of CH₄ hydrate in the absence of a vapor phase, i.e. the LH equilibrium, is shown above the VLH curve. The aqueous solubility of CH₄ at the vapor-liquid water (VL) equilibrium is shown below the VLH curve.

The WVU model was ported into MATLAB to enable incorporation into Ira Leifer's bubble plume propagation model developed in MATLAB. The MATLAB thermodynamics model was optimized to achieve convergence in three orders of magnitude less time and now requires milliseconds per calculation. This was necessary for practical inclusion in the bubble plume model which calculates hydrate aqueous solubility data for the entire water column as complex lookup tables. A lookup table is necessary as several million solutions of the differential equation describing bubble evolution are conducted for each bubble in a bubble plume.

Hydrocarbon bubble transport and fate modeling

A primary result of this project was a significant improvement of the bubble transport and fate model of Team Member Ira Leifer to incorporate the effects of hydrates, including mixed hydrocarbon hydrates (sII or Type II). A flow schematic of the numerical bubble propagation model is shown in Figure 27, which can simulate deep-sea bubbles, where hydrates can form on the outside of rising hydrocarbon gas bubbles. Experiments at the HWTF demonstrated that the presence and coverage of hydrate skins controls bubble dissolution and that the dissolution rate is proportional to the aqueous solubility of the hydrate. Therefore, the WVU-NETL hydrate solubility MATLAB code was incorporated into Ira Leifer's bubble fate modeling MATLAB code. Results from this improved thermodynamic model are discussed below.

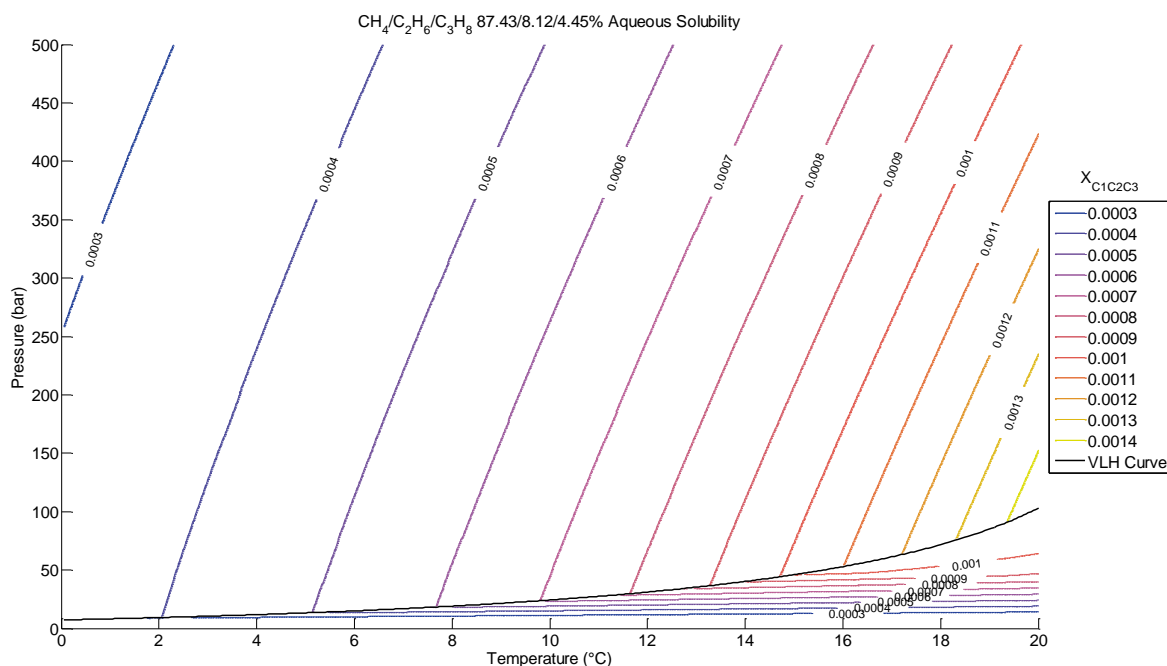


Figure 26. C1C2C3 in 35 salinity seawater phase diagram calculated with the WVU-NETL MATLAB model. The solid black line is the vapor-liquid water-hydrate (VLH) equilibrium curve, which is the lowest pressure/highest temperature at which hydrate is stable. The aqueous solubility of C1C2C3 hydrate in the absence of a vapor phase, i.e., the LH equilibrium, is shown above the VLH curve. The aqueous solubility of C1C2C3 at the vapor-liquid water (VL) equilibrium is shown below the VLH curve.

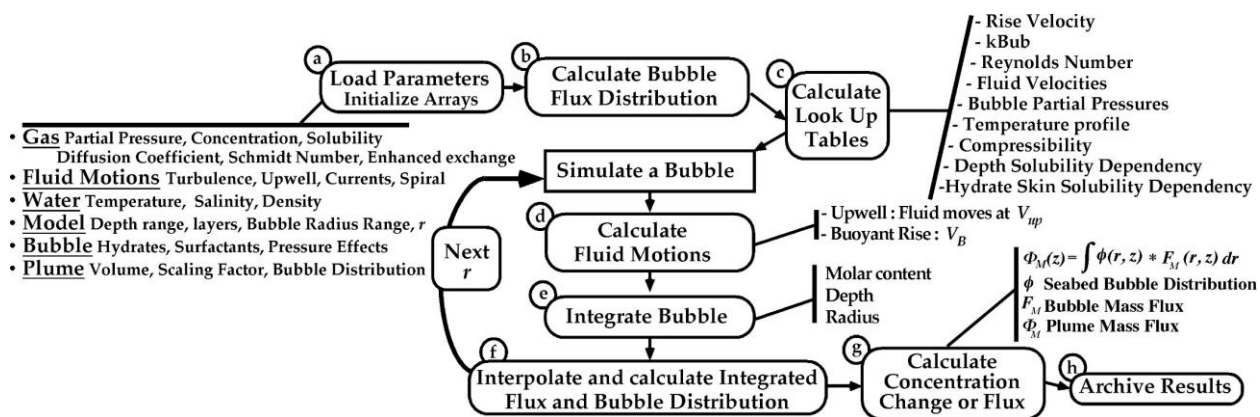


Figure 27. Model flow schematic providing an overview of the processes included in the model. (a) Input parameters include oceanic and hydrocarbon plume chemical and physical properties, and the (b) bubble size distribution and flux are interpolated into the model grid space. (c) Pre-computed look up tables of bubble transport-related chemical and physical parameters are used to achieve short model simulation times. Hydrate thermodynamics and solubility are pre-computed through an iterative process. Type II hydrate solubility vary with the evolving bubble composition and need to be calculated iteratively (not yet). (d-f) Simulation of each bubble in a size and depth class and integration to simulated plume characteristics. (g-h) The result is the mass flux of gas through the water column yielding the amount and percentage of gas transported to each depth in the oceanic water column.

For bubble transport modeling, the salient model features are that the thermodynamic model calculates the aqueous solubility, thermodynamic stability, and bulk composition of either pure or mixed hydrates. Importantly, the thermodynamic model, which has no fitting parameters, can calculate properties for thermogenic natural gas mixtures that are relevant to anthropogenic spills from industrial hydrocarbon extraction activities.

The hybrid thermodynamic-bubble fate model was able to explain the field data measured in the Gulf of Mexico during the HYFLUX campaign that showed C1-C5 gas bubbles from 890 m depth reaching the wave mixed layer with thermogenic gas reaching the ocean surface. Critically the HYFLUX field data require both sI methane and methane/ethane hydrates to explain an observed, deep gas intrusion layer as well as sII C1-C5 hydrates to explain an observed shallower gas intrusion layer. Furthermore, sII C1-C5 hydrates are key to explaining the transport of seabed gas to the sea surface. Validation with the field data demonstrates that the bubble-transport model, which contains no adjustable fitting parameters, correctly captures the real-world features affecting bubble fate and transport.

The main focus of the model results presented here is simulation of the HYFLUX campaign field experiment results, which were obtained at MC118 in the Gulf of Mexico (presented later in Figure 33). This is a unique data set, the only one in the world where aqueous gas concentration profiles for the entire water column were measured for a strong bubble plume.

The solubility of various gases in a hydrate-free bubble, including hydrocarbons up to pentane, and oxygen and nitrogen, which can dissolve into a bubble without a hydrate coating are shown in Figure 28. In this figure gas solubility is shown for bubbles without hydrate for a temperature profile measured at MC118 in the Gulf of Mexico during the HYFLUX experiment.

Laboratory experiments, as in the HWTF, often are with bubbles of a single size or limited size distribution. In contrast, natural seep bubble emissions always are distributed with size. Figure 29 depicts the size distribution measured at MC118 in the Gulf of Mexico.

Using the solubility data in Figure 28, the bubble size distribution data in Figure 29 and the seabed depth and temperature profile for MC118 (890 m) model simulations were conducted for the bubble plume observed at MC118. One of the advantages of numerical models is that they can explore what if questions of a non-physical nature, such as what if there were no hydrate skins on bubbles deep within the hydrate stability field?

Simulation results in the absence of hydrate bubble skins are shown in Figure 30 that depict the changes in gas concentration and gas flux with depth. Under these conditions virtually no gas remains undissolved above 725 m. Similarly, the modeling results in Figure 31 indicates that no seabed gas released at 890 m reaches the surface (right image). Looking at the fate of heavier molecules, like pentane, at a shallower depth of 600 m, only a few percent of pentane makes it to the surface in the absence of hydrates.

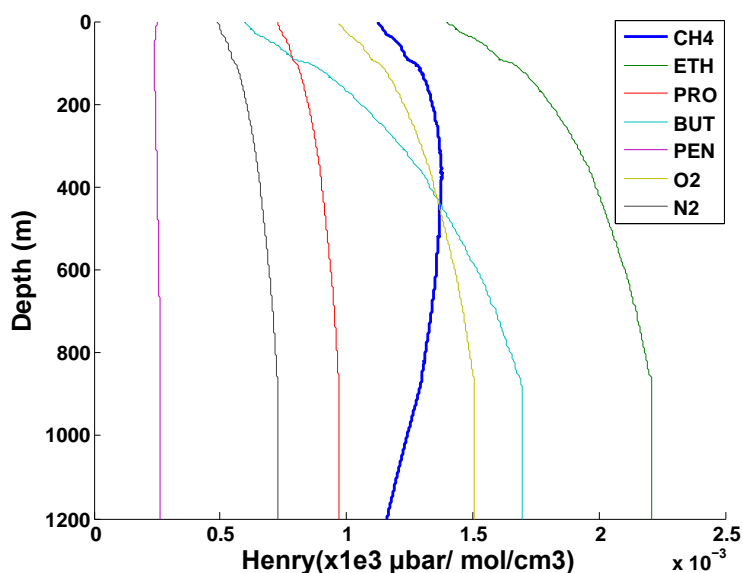


Figure 28. Gas solubility as a function of depth as represented by Henry's law constants accounting for pressure effects and temperature profile. As the seabed is at 890 m, deeper depths (non-physical) are represented as isothermal.

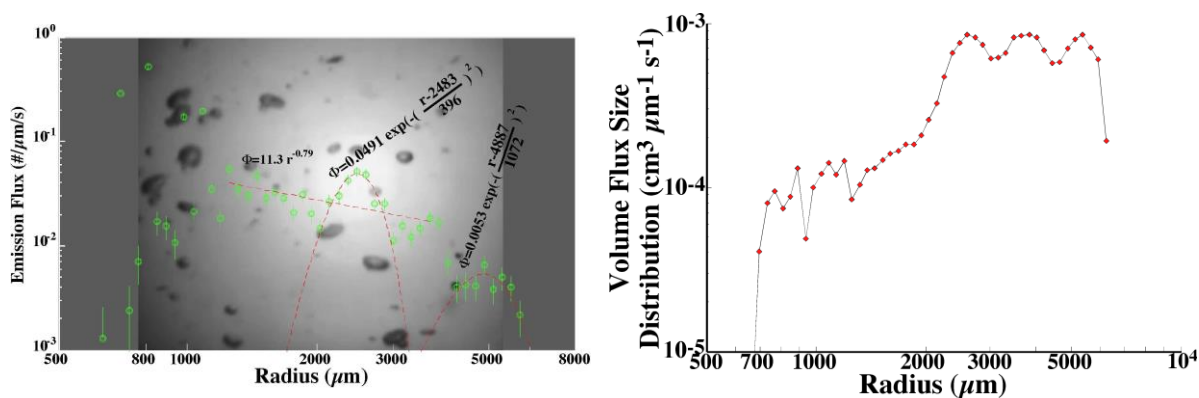


Figure 29. Bubble size distribution for the MC118 seep in the Gulf of Mexico. An image of the actual bubbles are shown on the left. The bubble volume size distribution is shown on the right.

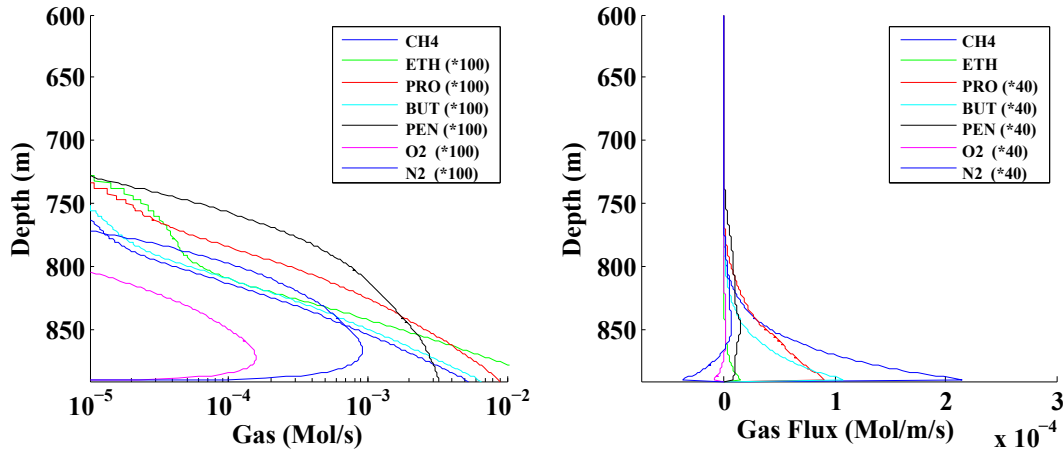


Figure 30. Modeling results for the bubble plume observed at MC118 showing the gas concentration (left) and flux (right) as a function of depth. These simulations assume no hydrate on the bubbles.

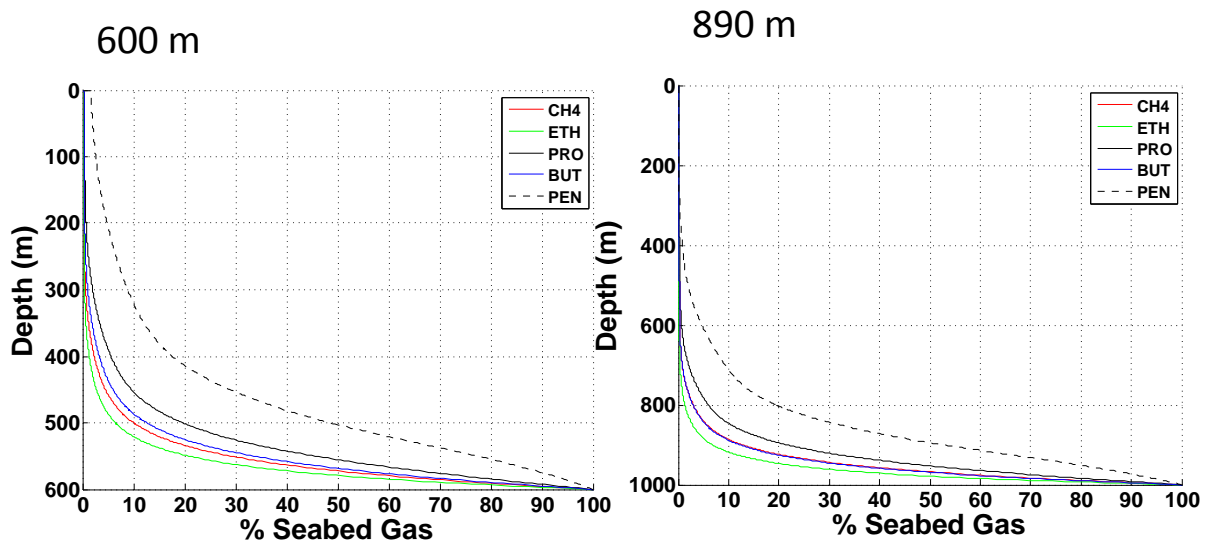


Figure 31. Model simulations for the bubble plume observed at MC118 at 600 m seabed depth (left) and 890 m seabed depth (right). These simulations assume no hydrate formation on the bubbles.

Figure 32 shows frames from an animation for a simulation of the MC118 bubble plume rising from a seep at 1000 m depth. The left frame contains information on the initial plume mass as a function of the seabed radius of bubbles in the plume. Also shown is the plume composition. The animation depicts changes in plume mass, bubble radius, and plume bubble composition (or content) as the bubbles rise (decreasing depth). The right frame is near the end of the simulation and shows that all but the very largest bubbles have dissolved by about 250 m. Moreover, the initially very large bubbles still remaining, dissolved shortly thereafter.

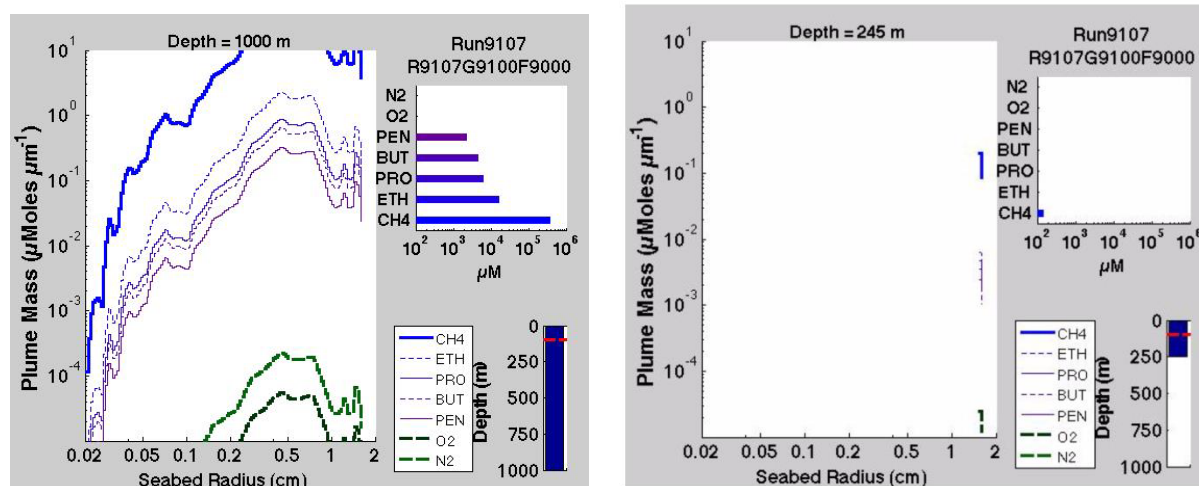


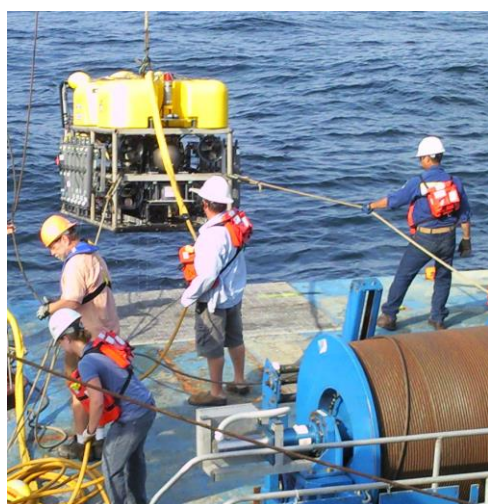
Figure 32. Images from the beginning (left) and near the end (right) of an animation showing the evolution of the composition and size distribution of a rising bubble plume in the absence of hydrates from 1000 m.

Figure 33 contains the field data for dissolved CH₄ and other hydrocarbons measured during the HYFLUX expedition. Two features are important that are not captured in the above model simulations without bubble hydrate skins:

- 1) Observed gas concentrations and gas concentration ratios are approximately independent of depth between 800 and 600 m. In the absence of hydrates, the dissolution of each hydrocarbon is controlled by its solubility and diffusivity and thus they should decrease approximately exponentially with depth. By comparison, a dissolving hydrate-covered bubble should lose mass based on the gas ratio in the hydrate cages of their hydrate skin due to dissociation of the cages.
- 2) Gas concentrations increase just above 300 m in an intrusion layer. This depth approximately corresponds to the top of the sII hydrate stability field. Model simulations without hydrate, fail to capture this observed intrusion layer.

The updated bubble model developed within this project incorporates the hydrate thermodynamic/solubility model for sI hydrates and sII hydrates, with hydrate solubility limiting gas bubble outgassing, a process that dominates in these deep bubbles with respect to the bubble dissolution rate. This is illustrated in Figure 34 by comparing the previous shown (Figure 28) solubility of gases in a bubble without hydrate on the left in this figure to those for the same bubble with a hydrate skin. Without hydrate (left) the gas solubility for each hydrocarbon species varies independently with depth (pressure); however, with hydrate (right) gas solubility is determined by thermodynamic equilibrium between the hydrate phase and the ocean, dramatically altering the distribution of the dissolution rates, and thus the gas depth profiles in the ocean water column. Therefore, the composition and ratio of the hydrocarbons in the hydrate phase determines the solubility of the hydrate at depths where hydrate is stable. At shallow depths hydrate no longer is thermodynamically stable and the gas phase determines solubility, resulting in a sharp increase in solubility and also dissolution flux, illustrated in Figure 34. The seabed for MC118 and these simulations is at 890 m, and solubility profiles here assume an

isothermal ocean at depths greater than 890 m for sensitivity studies projecting to deeper (and unphysical for MC118) depths.



ROV deployment in HYFLUX campaign

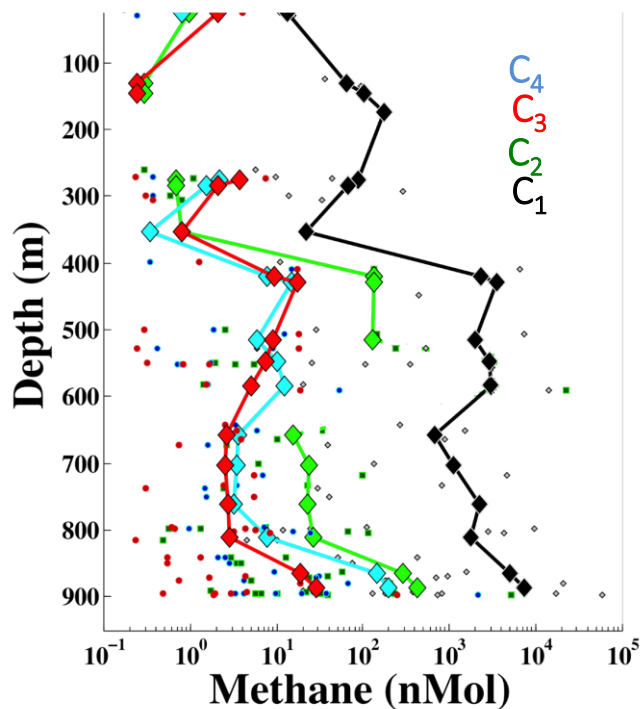


Figure 33. HYFLUX data from MC118, a natural seep with a seafloor depth of 890 m showing (right) aqueous molar gas concentrations throughout the water column determined from samples taken during the HYFLUX expedition. Also shown is the underwater vehicle (left) used to collect samples from which the data were obtained.

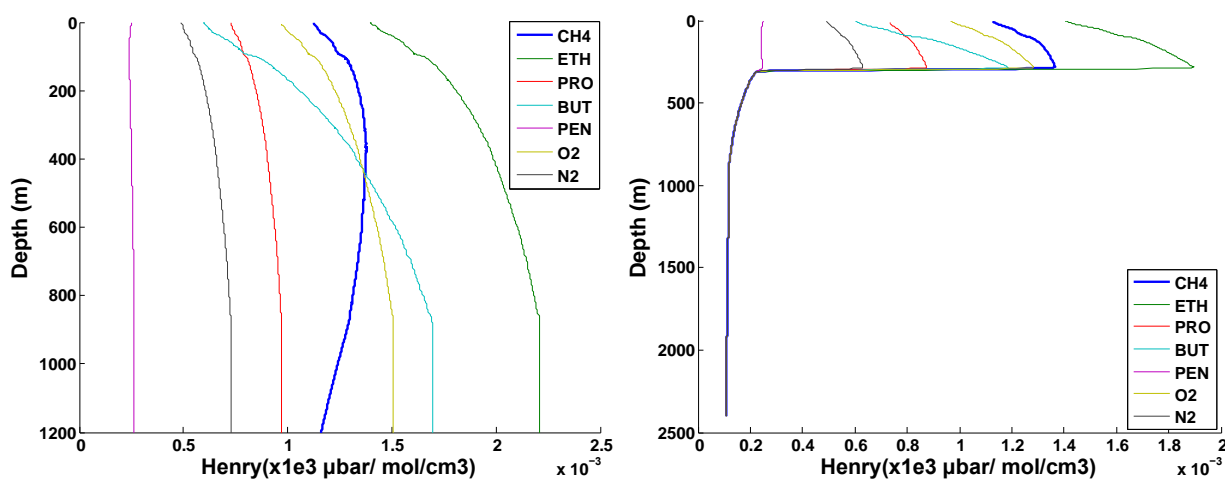


Figure 34. Gas solubilities (left) in the absence of hydrates and (right) with a sII hydrate skin.

In Figure 35, with structure II hydrates included, the model predicts an intrusion layer well below the thermocline, validated by HYFLUX data previously shown in Figure 33. In addition, Figure 35 shows that the model predicts bubbles will reach the thermocline (~ 70 m) and the sea surface even for this minor plume, and bubbles were tracked during HYFLUX to 70 m depth. Furthermore, water samples collected in a grid to 100 m depth showed thermogenic gases, i.e., methane and higher hydrocarbons. The sudden increase in solubility of hydrocarbons when the hydrate phase on the surface of a bubble becomes thermodynamically unstable and dissociates produces the intrusion layer. Just as a snowball does not instantly melt on a hot day, hydrate dissociation occurs with a stochastic delay that requires some time/rise distance. This results in an intrusion layer with a thickness of 10s of meters. In some waters, particularly Arctic, the top of the sII hydrate stability field may reach the thermocline where temperatures rise rapidly.

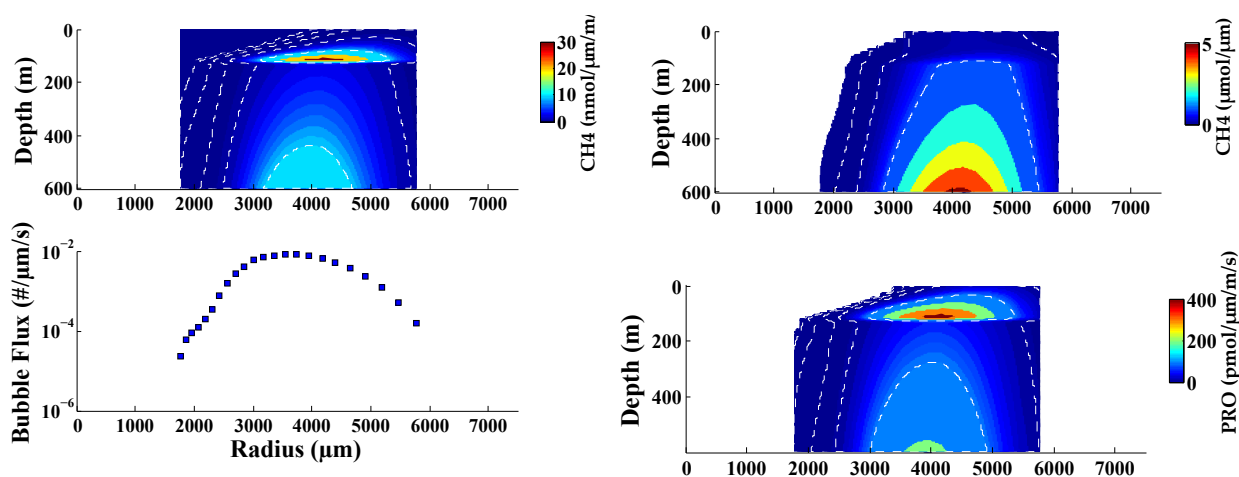


Figure 35. Modeling results for a minor plume that shows (bottom left) bubble size distribution and (top left) the formation of a CH₄ intrusion with hydrate. The CH₄ concentration without hydrate (upper right) has no such intrusion. A propane intrusion layer caused by sII hydrate (lower right).

The exact melting and intrusion depths are less important than the salient feature that absent sII hydrate thermochemistry, one cannot explain the intrusion at these depths. Moreover, sII hydrates enable the bubble plume to transport significant (non-negligible) methane and other contents to quite shallow water depths, which if less than the winter mixed wave layer will be efficiently transferred into the atmosphere during large storms – microbial degradation has time scales in the upper water column of more than a year. Given that Gulf hurricanes mix waters down to a couple of hundred meters, much of the contents of this intrusion layer will reach the atmosphere.

To summarize, sII hydrates allow a non-negligible fraction of the seabed gas to be transported into the atmosphere. In addition to global warming implications from the potent greenhouse gas, methane, there are significant implications for predicting the fate of oil on the bubbles and for toxic gas components that pose risks to responders.

Figure 36 depicts modeling results showing the depth evolution of the bubble size distribution for a minor and major bubble plume as bubbles in the plumes both rise and dissolve and grow

from hydrostatic pressure and air uptake. As expected, larger bubbles in the plume are more likely to reach the thermocline, and thus bubble plumes with a greater population of larger bubbles are more important to upwards methane transport in the water column. Figure 37 shows modeling results that compare gas content (left images) and transport or flux (right images) in a major plume with sII hydrate skins on the bubbles. Note the prominent gas intrusion layer in the right images that is formed once the hydrates dissociate at ~300 m depth and dissolution increases dramatically.

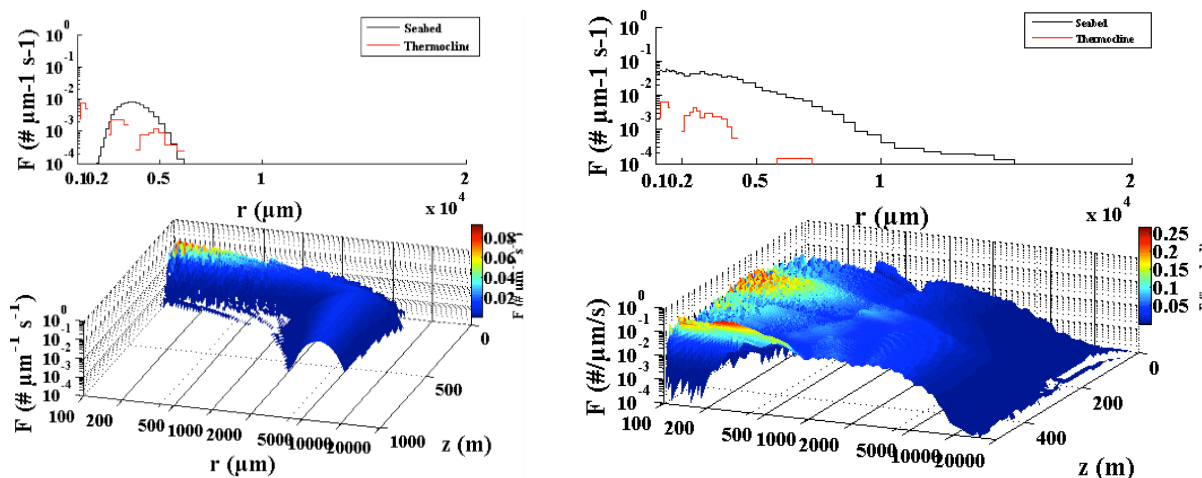


Figure 36. Simulation results for (left) minor and (right) major hydrocarbon bubble plumes containing bubbles with sII hydrate skins.

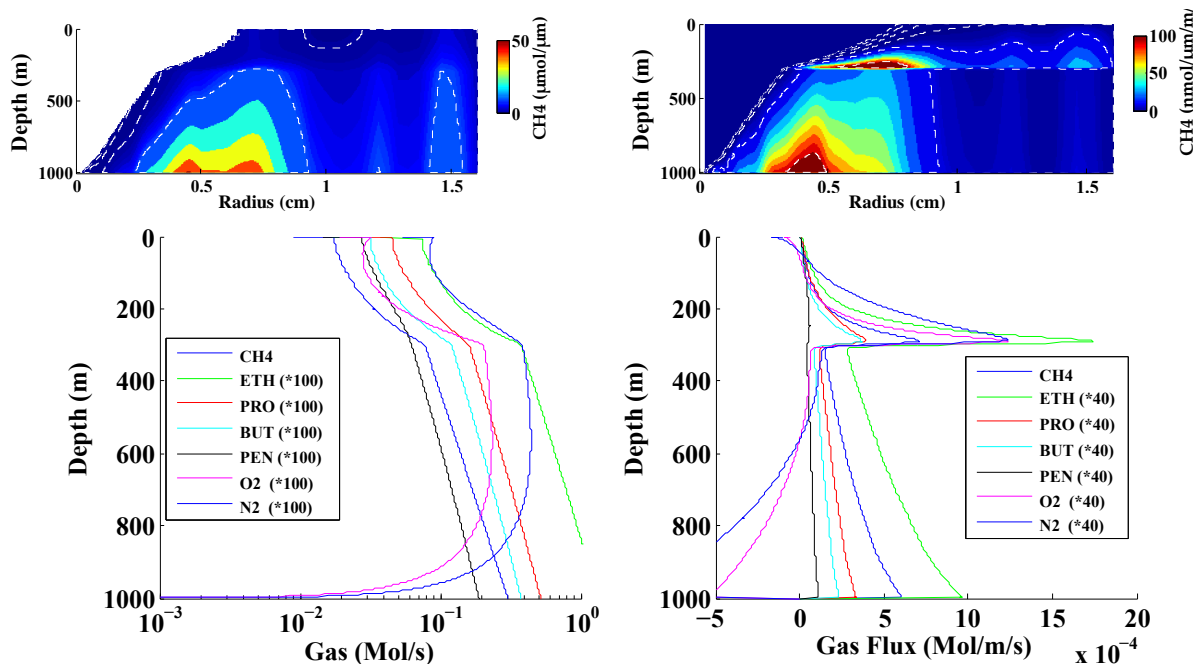


Figure 37. Simulations of a major plume with sII hydrate bubble skins. Left panels show gas content. Right panels show gas flux (dissolution). A CH₄ intrusion is visible in the figures on the right.

Figure 38 contains modeling results that compare gas transport efficiency to the atmosphere for a major bubble plume release at 1000 m depth with (left image) and without (right image) sII hydrate skins on the plume bubbles. The results show that about 30% of the seabed gas reaches the thermocline, about 5% of the seabed CH₄ and about 10% of the seabed propane reaches the surface due to sII hydrated bubbles (left image). When the model is run without hydrate (right image) all of the gas dissolves in the deep sea at depths close to the release depths; i.e., less than 10% of the seabed non-CH₄ hydrocarbon species rise more than 150 m by which depth half the CH₄ has dissolved.

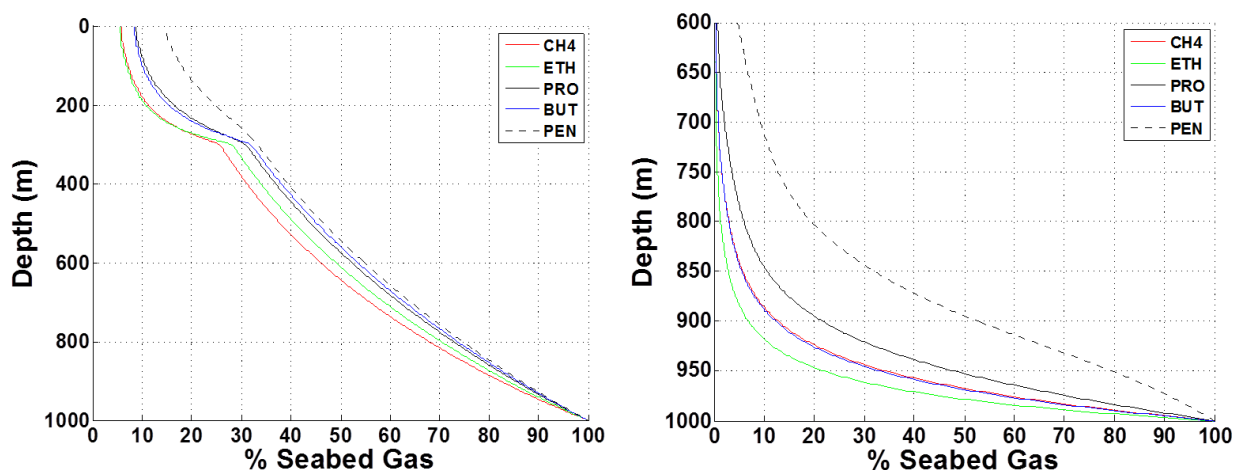


Figure 38. Modeling results for a major plume released at 1000 m depth. (Left) sII hydrate skins on bubbles and (right) no hydrates.

Figure 39 compares images from the beginning (left image) and near the end (right image) of an animation of a modeling simulation similar to that shown in Figure 32 only in this case with sII hydrate skins forming on the bubbles. The presence of hydrates at the depths shown reduces solubility and therefore dissolution rates, allowing bubbles to persist to shallow depths. At 95 m (approximate thermocline depth during HYFLUX) bubbles that were larger than 5 mm radius at the seabed continue rising towards the surface. The fraction of gas in the bubbles at this depth then would be transferred to the atmosphere directly or indirectly – as noted above, winter storms will sparge CH₄ and other hydrocarbons that were deposited even at deeper depth, transferring them to the atmosphere.

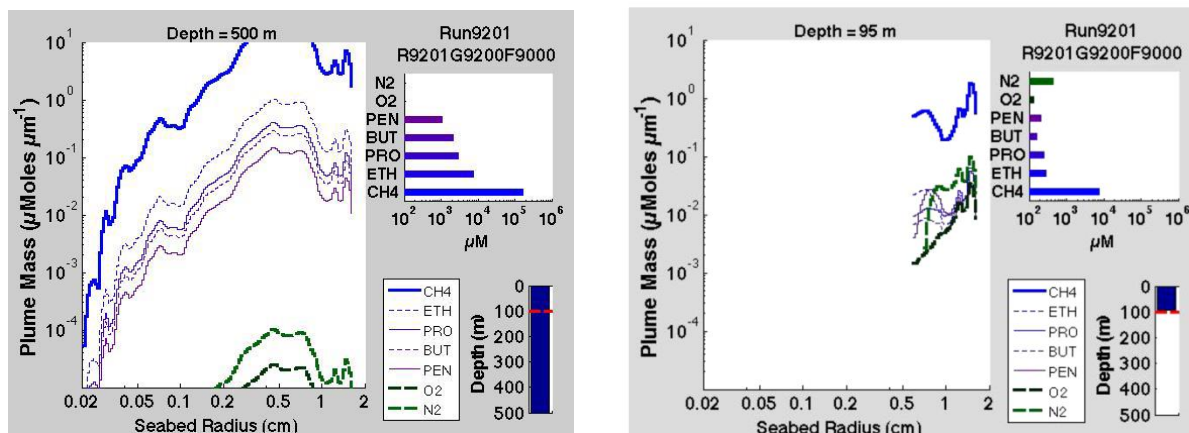


Figure 39. Images from the beginning (left) and near the end (right) of an animation showing the evolution of the composition and size distribution of a rising bubble plume in the absence of hydrates from 1000 m. .

Thus, the measured gas intrusion layer at ~150 to 300 m in the HYFLUX data is correctly predicted by the bubble plume model when the new sII hydrate data from thermodynamic modeling are used to predict the stability of surficial hydrate on the plume bubbles. This is clearly shown by combining data shown in previous figures in Figure 40. Without hydrate bubble skins, no intrusion layer was predicted as previously evidenced in the right pane of Figure 30.

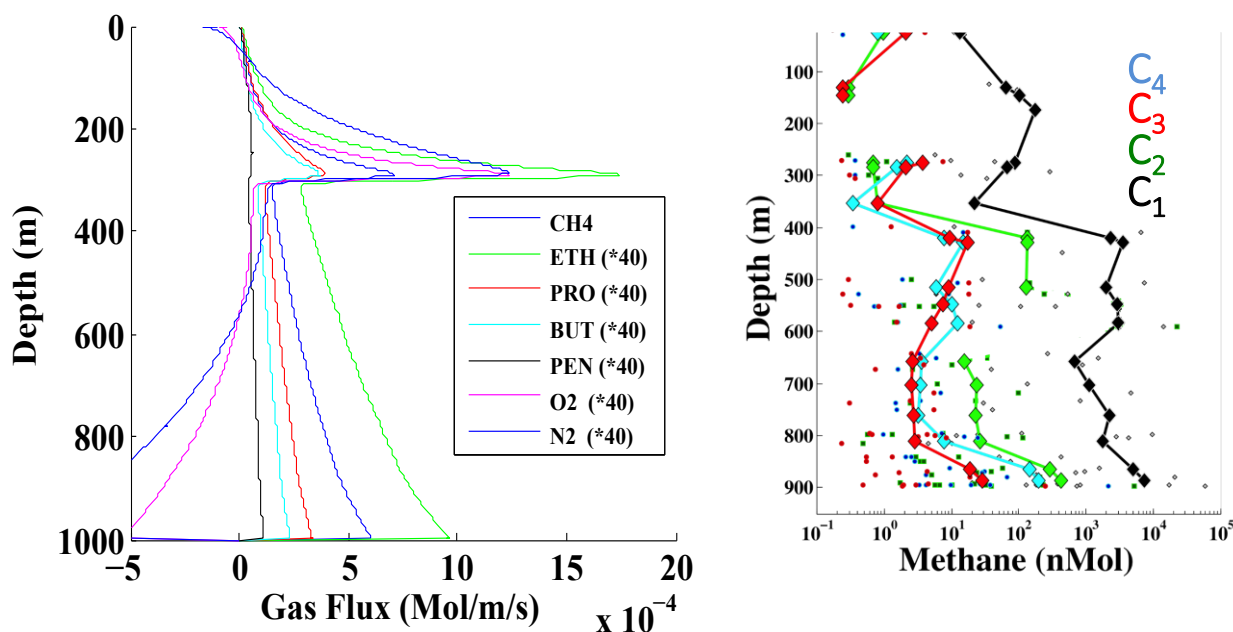


Figure 40. Comparison of (left) model prediction of gas flux and (right) the intrusion layer determined at the thermocline from the HYFLUX data.

Figure 41 compares modeling results for plumes released at different depths with the same bubble number and size distribution as used in the HYFLUX simulations. These results show that deeper bubbles transfer more gas to the surface. This is because gas density increases sharply with depth, and thus the same volume bubble has more moles of gas at 1000m than 400m. Because more gas is present initially, although the deeper bubbles lose a higher percentage of gas before reaching the depth at which hydrate begins to decompose (~300 m in this simulation), they contain more gas at the top of the hydrate stability field than bubbles released at shallower depths. Thus, bubbles released at deeper depths are larger when they arrive at the depth at which hydrate begins to dissociate, and this allows a higher percentage of the gas in these bubbles to reach the atmosphere as larger bubbles are more efficient at mass transport than smaller bubbles.

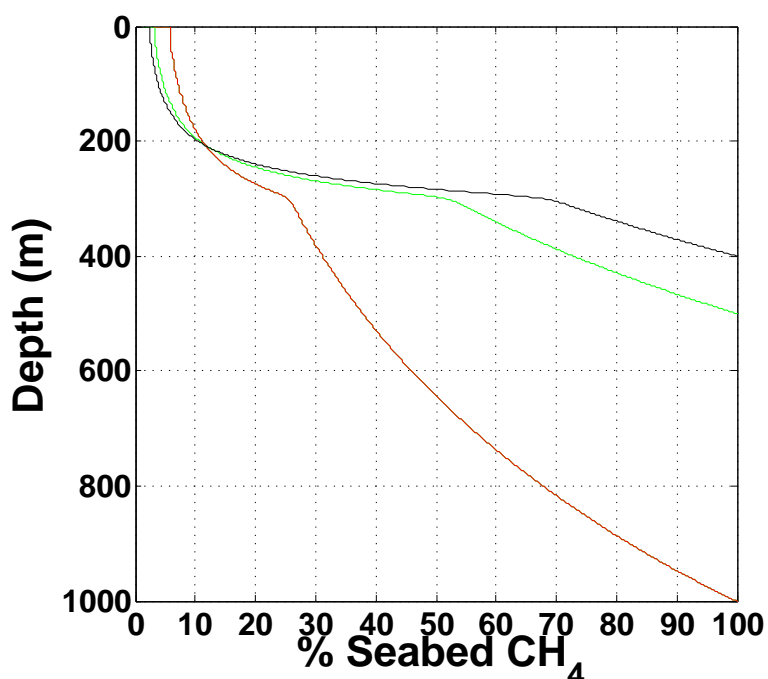


Figure 41. Modeling results for plumes released at different depths with the same bubble number and size distribution. Bubbles at 100% seabed CH₄ are at their release depth.

The modeling results shown here clearly demonstrate that inclusion of sII hydrate-covered bubbles are required to predict correctly the field data previously obtained in the HYFLUX project. This first-order effect needs to be included in deep-sea bubble plume modeling to predict gas transport and bubble fate correctly.

Prediction of sII hydrate effects on bubble plumes was made possible by the thermodynamic modeling performed by Team members on this project. The dramatic effect discussed above is a major first step in developing improved models to predict the fate of fluids released from subsea eruptions, leaks, and seeps, both for determining response measures, development of prevention strategies, and for quantifying atmospheric greenhouse gas contributions.

Finally, the main emphasis of this research has been forward looking in the development of improved bubble plume models, specifically those that incorporate sII hydrate effects. The figures in this section demonstrate our success in this effort. However, reexamination of the data obtained by *Camilli et al.* (2010), during the Deepwater Horizon oil spill reveal that similar intrusions of C2 and C3 hydrocarbons occurred, but were not commented on at that time. Figure 41 depicts these data, which show intrusions of these species at depths near 200 to 300 m that can only be explained by models incorporating sII hydrate bubble thermodynamics.

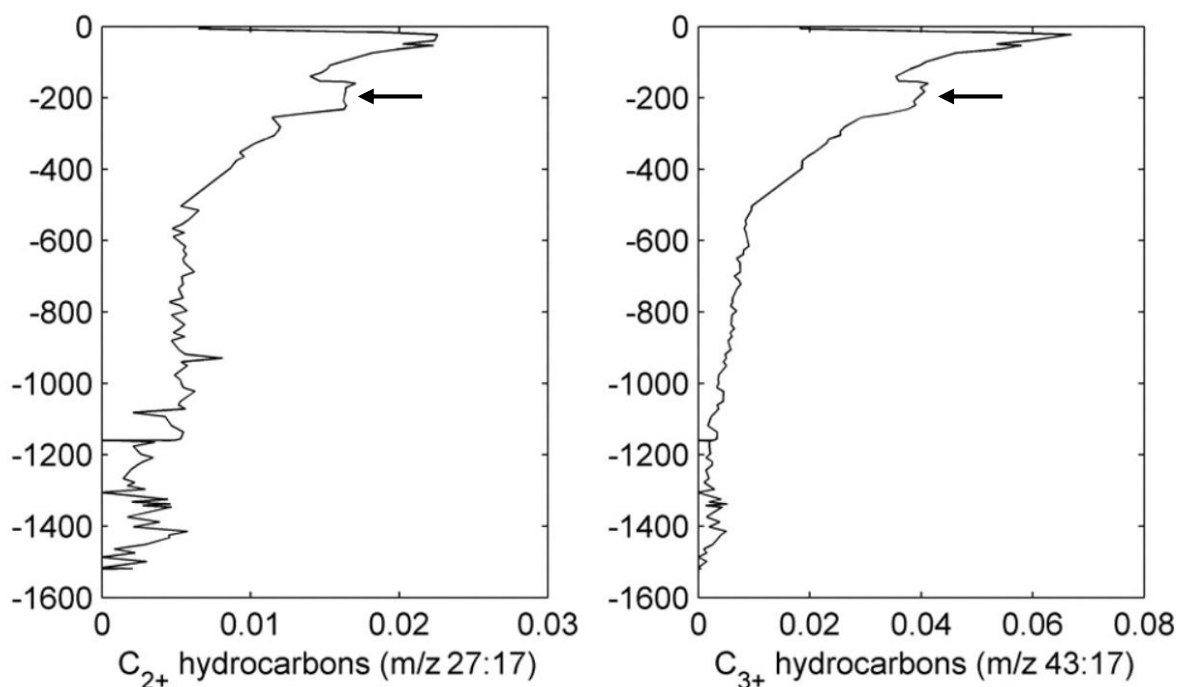


Figure 41. Data from Figure 1 in *Camilli et al.* (2010) showing the intrusion of C2 and C3 hydrocarbons into the Gulf of Mexico from the Deepwater Horizon oil spill as measured by

Research Needs

The modeling and experimental results presented in this report have made possible the development of an improved bubble plume model that can reproduce observed field data characteristics, unlike previous models that do not incorporate correct hydrate thermodynamics.. As described in the previous section, the major advance was the correct incorporation of the first order effect of hydrate formation utilizing more complex gases that form sII hydrate skins on plume bubbles.

There are other chemical and physical processes that can affect bubble plume models and have yet to be resolved. These include:

- Implications of cracks in a hydrate skin and partial hydrate coverage on bubble gas diffusion (see Figures 20 and 22 above and *Warzinski et al.*, (2014)).
- Importance and influence of shedding or flaking of hydrate from a hydrated bubble.

- Mechanism of hydrate skin or plate dissociation (mono-layer or multi-layer) and bubble gas diffusion.
- Stochastic formation and dissociation processes, i.e., sub-cooling, over-pressurization, and/or supersaturation.
- Dissolved air gases and their influence on hydrocarbon gas transport; does uptake of these gases occur?
- Surfactant effects on hydrate formation and structure and stability.
- Dispersant effects on hydrate formation, stability and gas transport.

The research on this project has bearing on several of the above processes. The discovery of relationships between partial hydrate coverage on a bubble, its hydrodynamics, and dissolution behavior was not even postulated prior to this work. Also, the discovery of similarities of changing hydrate morphology on a bubble to large-scale interactions of sea ice and waves is a new insight that opens a pathway to new approaches for refining plume models.

Considering the accomplishments in both the experimental and modeling research reported here, the following concepts would be useful to pursue in the future to continue the development of better plume models:

- Incorporation of gas analysis in the HWTF. The ability to analytically determine the partitioning of gas as a mixed-gas bubble dissolves in the HWTF (e.g., C1C2C3) is necessary for providing the type of information needed in a bubble plume model. This would ideally involve a two prong experimental approach. The first would be the use of standard analytical methodology to sample the aqueous phase in the HWTF while a bubble of gas is dissolving. A mass spectrometer could be incorporated into the flow loop to sample and analyze the gas in the water or seawater during bubble dissolution observations. Other techniques, such as head-space analysis should also be considered.

A second improvement would be the development of an approach to use laser Raman spectroscopy to analyze directly the contents of a bubble during observations in the HWTF. This would be a research effort; however, members of the Team have worked with the world-class Raman spectroscopy group at NETL and the technique looks feasible on both a sensitivity and time-scale basis. Success in this endeavor would be a very noteworthy accomplishment that could possibly be adapted to in-situ applications in the deep ocean.

- Bubble plume modeling utilization. The bubble plume model used and improved in this work needs to be made more accessible to parties that could use its output directly or integrated into larger scale ocean/atmospheric models. At present, the model was invented and developed by Dr. Ira Leifer over a number of decades, and allows the user to misuse it, producing non-physical results. Although it is possible to train others to run the model, it would be more efficient to develop a parameterized version that encompasses a wide range of simulations for environmental conditions that could be easily used by non-skilled users.
- Resolve discrepancies between laboratory and ocean results. It is the experience of Team members and others that the complexity of seawater exerts influences on bubble hydrate

formation and dissolution that are not exactly reproducible in the laboratory. Even in the work reported here, the in-situ dissolution results of *Rehder, et al.*, (2009) are from ~1.5 – 3 times higher. We are confident in the values obtained in the HWTF; however, the influence of biosurfactants and other substances in the deep ocean, and the experimental design in *Rehder, et al.*, (2009) cannot be determined without additional research both in the laboratory and in the deep ocean. This research would include the use of surfactants and other substances in the HWTF, perhaps even actual water from the deep sea, and a series of in-situ experiments in which HSHD videography are used in a device modeled after the HWTF that could be deployed from an ROV, following on the pioneering design of the HYFLUX campaign.

Publications and Presentations

The following manuscripts have been published in peer-reviewed journals:

K. Anderson¹, G. Bhatnagar¹, D. Crosby¹, G. Hatton¹, P. Manfield¹, A. Kuzmicki¹, N. Fenwick¹, J. Pontaza¹, M. Wicks¹, S. Socolofsky², C. Brady³, S. Svedeman³, A. Sum⁴, C. Koh⁴, J. Levine⁴, R. P. Warzinski⁵, and F. Shaffer⁵ (2012), “Hydrates in the Ocean–Beneath, Around, and Above Production Equipment,” *Energy & Fuels*, 26 (7), 4167-4176 .

¹Shell, ²Texas A&M, ³Southwest Research Institute, ⁴Colorado School of Mines, ⁵NETL

R. J. Lynn¹, I. V. Haljasmaa¹, F. Shaffer², R. P. Warzinski², J. S. Levine² (2014), “Automated Pitot Tube System for Millimeter-Resolution Low Velocity Profile Measurement in Water,” *Flow Measurement & Instrumentation*, 40, 2014, 50-57.

R. P. Warzinski¹, R. Lynn², I. Haljasmaa², I. Leifer³, F. Shaffer¹, B. J. Anderson⁴, J. S. Levine¹ (2014), “Dynamic Morphology of Gas Hydrate on a Methane Bubble in Water: Observations and New Insights for Hydrate Film Models,” *Geophysical Research Letters*, 41, 6841–6847, doi:10.1002/2014GL061665.

The following PhD thesis was completed with funding from this project:

S. C. Velaga, (2014), “Stability of Methane-Ethane-Propane Mixed Gas Hydrates under Deep Water Conditions,” 153 pp., West Virginia Univ., Morgantown, West Virginia. Open access link <http://gradworks.umi.com/3618152.pdf>.

The following manuscripts are in draft form as of this writing:

S. C. Velaga¹, J. S. Levine², R. P. Warzinski², B. A. Anderson¹, “A Thermodynamic Model to Predict the Aqueous Solubility of Hydrocarbon Mixtures at Two-Phase Hydrate – Liquid Water Equilibrium,” Target Journal: *Fluid Phase Equilibria*. ” (Final draft with coauthor’s comments completed)

J.S. Levine, I. Leifer, R. Lynn, F.D. Shaffer, R.P. Warzinski, I. Haljasmaa, “A New Method for Determining the Size of Oblate Spheroidal Bubbles.” Target Journal: *Experimental & Thermal Science*. ” (A draft manuscript has been prepared)

Solomon, E.¹, I. Leifer, M. Kastner², J. Levine, and G. Rehder³ (2013), “A reassessment of deep sea seepage and atmospheric budgets: Type 2 hydrate-mediated bubble transport,” Target Journal: *Nature*

¹Univ. of Washington, ²Scripps, ³Univ. of Warnemunde

The following presentations were made at scientific and engineering meetings:

I. Leifer, “Reassessment of Deep Methane Contribution to the Atmosphere: The Hydrated Bubble Plume Express,” 2014 Gordon Research Conference on Natural Gas Hydrate Systems, Symposium on Gas Hydrates, Permafrost, and Seeps, March 23-28, 2014, Galveston, Texas.

R. P. Warzinski¹, R. Lynn², I. Haljasmaa², I. Leifer^{3,4}, F. Shaffer¹, B. J. Anderson⁵, J. S. Levine¹, “The Role of Gas Hydrates during the Release and Transport of Well Fluids into the Deep Ocean,” 2014 Clean Gulf Conference, December 3-4, 2014, San Antonio, Texas.

References

- Camilli, R., C. M. Reddy, D. R. Yoerger, B. A. S. Van Mooy, M. V. Jakuba, J. C. Kinsey, C. P. McIntyre, S. P. Sylva, J. V. Maloney (2010), “Tracking hydrocarbon plume transport and biodegradation at Deepwater Horizon,” *Science*, 330, 201-204, doi: 10.1126/science.1195223.
- Haljasmaa, I. V., J. S. Vipperman, R. J. Lynn, R. P. Warzinski (2005), “Control of a fluid particle under simulated deep-ocean conditions in a high-pressure water tunnel,” *Review of Scientific Instruments*, 76, 025111, <http://dx.doi.org/10.1063/1.1854216>.
- Haljasmaa, I. V. (2006), On the drag of fluid and solid particles freely moving in a continuous medium, Ph.D. thesis, 185 pp, University of Pittsburgh, Pittsburgh, Pennsylvania.
- Holder, G., G. Corbin, K. Papadopoulos (1980), “Thermodynamic and molecular properties of gas hydrates from mixtures containing methane, argon, and krypton,” *Industrial & Engineering Chemistry Fundamentals*, 19, 282, doi: 10.1021/i160075a008.
- Lu, W., I. M. Chou, and R. C. Burruss (2008), Determination of methane concentrations in water in equilibrium with sI methane hydrate in the absence of a vapor phase by in situ Raman spectroscopy, *Geochimica et Cosmochimica Acta*, 72(2), 412-422, doi:10.1016/j.gca.2007.11.006.
- MacDonald, I. (2011) “Remote sensing and sea-truth measurements of methane flux to the atmosphere (HYFLUX project),” Final Report, DE-NT0005638, available National Energy Technology Laboratory, 164 pp.
- Rehder, G., I. Leifer, P. G. Brewer, G. Friederich, and E. T. Peltzer (2009), Controls on methane bubble dissolution inside and outside the hydrate stability field from open ocean field experiments and numerical modeling, *Marine Chemistry*, 114(1-2), 19-30, doi: 10.1016/j.marchem.2009.03.004.
- Sloan, E. D., and C. A. Koh (2008), *Clathrate Hydrates of Natural Gases*, 3rd ed., 721 pp., CRC Press, Boca Raton, Florida, USA, ISBN-10:0-8493-9078-8.
- Smith, O. P. (2000), Observers guide to sea ice, US Dept. of Commerce, National Oceanic and Atmospheric Administration, National Ocean Service, Office of Response and Restoration, National Environmental Satellite, Data, and Information Service, National Ice Center.

- Van der Waals, J. H., J. C. Platteeuw, (1959), Clathrate Solutions, in *Advances in Chemical Physics*, 2, ed. I. Prigogine, John Wiley & Sons, Inc., Hoboken, New Jersey, doi: 1002/9780470143483.ch1.
- Warzinski, R. P., D. E. Riestenberg, J. Gabitto, I. V. Haljasmaa, R. J. Lynn, and C. Tsouris (2008), Formation and behavior of composite CO₂ hydrate particles in a high-pressure water tunnel facility, *Chemical Engineering Science.*, 63(12), 3235-3248, doi: 10.1016/j.ces.2008.03.005.
- Warzinski, R. P., R. Lynn, I. Haljasmaa, I. Leifer, F. Shaffer, B. J. Anderson, J. S. Levine (2014), “Dynamic Morphology of Gas Hydrate on a Methane Bubble in Water: Observations and New Insights for Hydrate Film Models,” *Geophysical Research Letters*, 41, 6841–6847, doi:10.1002/2014GL061665. (Open Access)

Abbreviations and Symbols

a	Major radius of an ellipsoidal bubble
b	Minor radius of an ellipsoidal bubble
BSEE	Bureau of Safety and Environmental Engineering
C1C2C3	8.121% ethane, 4.448% propane, balance methane gas mixture ($\pm 1\%$)
CH ₄	99.99% methane
CHR	Center for Hydrate Research
CSM	Colorado School of Mines
DP	Distributor plate, i.e., the parts of the WT that join VS to VS and VS to SS
EPAct	Energy Policy Act of 2005
HSHD	High-speed, high-definition (in this work 2560 X 1680, 195 frames/s)
exp	Experimental condition
HWTF	High-Pressure Water Tunnel Facility
LH	Liquid/Hydrate equilibrium
MSI	Marine Science Institute
NETL	National Energy Technology Laboratory
ORD	Office of Research and Development
ORISE	Oak Ridge Institute of Science and Education
P	Pressure
T	Temperature
R	Bubble radius
R_e	Equivalent spherical radius of a bubble
RO	Reverse osmosis
RUA	Regional University Alliance
sI	Structure I hydrate forming gas (same as Type I)
sII	Structure II hydrate forming gas (same as Type II)
SS	Stilling section, i.e., the part of the WT where water flow is conditioned
WVU	West Virginia University
UCSB	University of California Santa Barbara
URS	URS Corporation
VL	Vapor/Liquid equilibrium
VLH	Vapor/Liquid/Hydrate equilibrium (or V-Lw-H)
VS	Viewing section, i.e., the part of the WT containing viewing windows
X	Concentration of dissolved gas
WT	Water tunnel, i.e., the main vessel in the HWTF
X_{CH_4}	Concentration of dissolved methane as mole fraction